

34 **Abstract**

35 Macrophage infectivity potentiator (MIP) proteins are widespread in human pathogens including
36 *Legionella pneumophila*, the causative agent of Legionnaires' disease and protozoans such as
37 *Trypanosoma cruzi*. All MIP proteins contain a FKBP (FK506 binding protein)-like prolyl-*cis/trans*-
38 isomerase domain that hence presents an attractive drug target. Some MIPs such as the *Legionella*
39 *pneumophila* protein (*LpMIP*) have additional appendage domains of mostly unknown function. In full-
40 length, homodimeric *LpMIP*, the N-terminal dimerization domain is linked to the FKBP-like domain
41 via a long, free-standing stalk helix. Combining X-ray crystallography, NMR and EPR spectroscopy
42 and SAXS, we elucidated the importance of the stalk helix for protein dynamics and inhibitor binding
43 to the FKBP-like domain and bidirectional crosstalk between the different protein regions. The first
44 comparison of a microbial MIP and a human FKBP in complex with the same synthetic inhibitor was
45 made possible by high-resolution structures of *LpMIP* with a [4.3.1]-aza-bicyclic sulfonamide and
46 provides a basis for designing pathogen-selective inhibitors. Through stereospecific methylation, the
47 affinity of inhibitors to *L. pneumophila* and *T. cruzi* MIP was greatly improved. The resulting X-ray
48 inhibitor-complex structures of *LpMIP* and *TcMIP* at 1.49 and 1.34 Å, respectively, provide a starting
49 point for developing potent inhibitors against MIPs from multiple pathogenic microorganisms.

50

51

52 **Key Words:** virulence factor; protein inhibitor complex; protein dynamics

53

54

55 Introduction

56 Bacterial parasitism is a wide-spread phenomenon and a serious health concern [1]. Approximately half
57 of all identified *Legionella* species are associated with human disease, but most human legionellosis are
58 caused by *Legionella pneumophila* [2]. In their natural fresh water reservoir habitat, these facultative
59 intracellular gram-negative bacteria infect protozoa, where, protected from harsh environmental
60 conditions, they find optimal conditions for intracellular replication while benefiting from the nutrient
61 supply provided by the host [3]. After aspiration of contaminated water from e.g. air conditioners or hot
62 water cisterns, *L. pneumophila* can also invade alveolar macrophages in the human lung thereby
63 mimicking the infection of its native amoebal host [2,4,5]. This may result in severe infections such as
64 Legionnaires' disease or the more benign Pontiac disease [2,4]. Although *Legionella* infections can be
65 treated with antibiotics, Legionnaires' disease nonetheless has a mortality rate of ~10%, which is likely
66 even higher in older or immunocompromised patients [6].

67 To promote uptake into a host cell, *L. pneumophila* relies on a number of proteins, including MIP
68 (Macrophage infectivity potentiator), the first identified *L. pneumophila* virulence factor [7–9].
69 *Legionella pneumophila* MIP (*LpMIP*) improves the environmental fitness of the bacterium and
70 facilitates the progression of the early stages of the intracellular infection cycle [9–11]. Genetic deletion
71 of *LpMIP* results in a reduced intracellular replication rate [9,12].

72 *LpMIP* is a homodimeric protein consisting of an N-terminal dimerization domain, a 65 Å long, free-
73 standing α -helix, the “stalk helix”, and a C-terminal peptidyl prolyl-*cis/trans*-isomerase (PPIase)
74 domain [13–15]. Structurally, the PPIase domain belongs to the FK506-binding proteins (FKBPs)
75 named after their interaction with the natural product macrolide lactone FK506 [16,17]. In FKBPs, an
76 amphipathic five-stranded β -sheet wraps around an α -helix thus forming a hydrophobic cavity that binds
77 substrates and inhibitors [18]. Although the molecular mechanism of *LpMIP* action in infection and its
78 molecular target(s) remain unclear, it was implicated in host collagen interaction and subsequent
79 epithelial barrier transmigration [19,20]. Nonetheless, the interaction between *LpMIP* and collagen
80 could not be mapped in detail, and instead of using classic chemical shift perturbations (CSP), NMR
81 (nuclear magnetic resonance) spectroscopic PREs (paramagnetic relaxation enhancement) of spin-
82 labeled collagen peptides had to be used to detect binding to *LpMIP* [19], suggesting weak binding
83 affinities. In contrast, unambiguous binding site mapping to *LpMIP* has been shown by NMR CSP for
84 rapamycin, a macrolide which also inhibits human FKBPs [21].

85 MIP proteins are widely expressed in many other human pathogenic microorganisms such as *Chlamydia*
86 *spp.* [22], *Neisseria gonorrhoeae* [23], the entero-pathogen *Salmonella typhimurium* [24], *Pseudomonas*
87 *aeruginosa* [25], and intracellular parasitic protozoans such as *Trypanosoma cruzi*, the causative agent
88 of Chagas disease in South and Central America [26–28]. Hence, the PPIase domains of MIP proteins
89 are attractive antimicrobial and antiparasitic drug targets [29], however their shallow ligand binding
90 pocket and similarity to human FKBPs render selective drug design challenging [30,31]. No structures
91 of a *Legionella* MIP with a synthetic inhibitor are available to date and, in the absence of a high-

92 resolution structure of a microbial MIP and human FKBP MIP in complex with the same synthetic
93 inhibitor, no side-by-side structural comparison is currently possible.

94 Limited structural information of *LpMIP* is available, with only a crystal structure of the *apo* full-length
95 homodimer (PDB: 1FD9) [14] and the NMR solution structures of an *apo* and rapamycin-bound
96 truncation mutant (PDB: 2UZ5, 2VCD) [21]. This construct, *LpMIP*⁷⁷⁻²¹³, comprises the C-terminal half
97 of the stalk helix followed by the FKBP-like domain and thus resembles the architecture of the
98 constitutively monomeric *T. cruzi* MIP protein [26]. Other pathogens such as *Burkholderia*
99 *pseudomallei*, the bacterium causing melioidosis, express even more minimalistic MIP proteins, lacking
100 both dimerization domain and the complete stalk helix [32,33].

101 The role of MIP appendage domains, or the consequences of their (partial) absence, remains unclear.
102 However, homodimeric, full-length MIP from *Legionella pneumophila* presents a unique opportunity
103 to explore the role of these domains in conformational flexibility and inhibitor binding. Here, we
104 combined X-ray crystallography, small angle X-ray scattering (SAXS), nuclear magnetic resonance
105 (NMR) and electron paramagnetic resonance (EPR) spectroscopy to uncover the importance of the
106 *LpMIP* stalk helix for the protein's functional dynamics and to identify similarities and differences in
107 inhibitor binding among MIP proteins from various human pathogenic microorganisms and human
108 FKBP.

109

110 **Results**

111 **Structural dynamics of full-length *LpMIP* and consequences of inhibitor binding**

112 Comparing our crystal structure of homodimeric full-length *LpMIP* with improved resolution (1.71 Å,
113 PDB: 8BJC) to the previously published one (2.41 Å, PDB: 1FD9 [14]), revealed a ~18° splay between
114 the stalk helices in the two structures (Fig. 1A, B). The higher resolution of our electron density map
115 allowed unambiguous placement and assignment of all stalk helix residues (Fig. 1C, Table S1).
116 Furthermore, the stalk helix is not involved in crystal contacts suggesting that intrinsic conformational
117 heterogeneity is responsible for the observed differences between the two structures.

118 The splaying of the stalk helix, which emanates from the mid-helix residues ⁷⁶EFNKK⁸⁰, results in a
119 relative reorientation of the attached FKBP-like domains in the two crystal structures. Nonetheless, both
120 globular domains align with an RMSD of 0.214 Å (Fig. 1D). The main structural differences between
121 the two FKBP-like domain structures were observed in the loop between β-strand 4 and 5, resulting in
122 a different side-chain orientation for residue S189. Minor side-chain rearrangements were also seen for
123 residues D142, V158 and Y185 in the active site which may however result from the different
124 resolutions of the two structures.

125

126 Although microbial MIP proteins are promising drug targets, the structural similarity to human FKBP
127 proteins raises concerns about possible cross-reactivity and off-target effects [34,35]. Naturally
128 occurring inhibitors such as rapamycin (sirolimus) are large and chemically complex, poorly soluble in

129 water, and have severe immunosuppressive effects limiting their use to treat microbial infection [36].
130 The comparison of human FKBP and pathogenic microbial MIP proteins bound to a chemically simpler,
131 synthetic inhibitor molecules could thus present an important step towards improving ligand selectivity.
132 Recently, an inhibitory effect of [4.3.1] bicyclic sulfonamides on *L. pneumophila* proliferation in
133 macrophages was demonstrated [34]. One such molecule, (1S,5S,6R)-10-((3,5-
134 dichlorophenyl)sulfonyl)-5-(hydroxymethyl)-3-(pyridin-2-ylmethyl)-3,10-diazabicyclo [4.3.1]decan-2-
135 one (JK095, Scheme 1), was co-crystallized with a human FKBP51 domain construct [34]. We thus
136 deemed this compound a promising candidate for structural studies with MIP proteins from human
137 pathogens and downstream structural comparison with human FKBP. Isothermal titration calorimetry
138 (ITC) confirmed that JK095 indeed interacts with microbial MIP proteins and *LpMIP* variants (see
139 below) and binds to full-length *LpMIP* with a dissociation constant of $1.27 \pm 0.14 \mu\text{M}$ (Fig. S1).
140 We also determined the structure of full-length *LpMIP* in complex with JK095 by X-ray crystallography
141 at 2.4 Å resolution (PDB: 8BJD) (Fig. 2A). The most notable structural differences between the crystal
142 structures of *apo* and JK095-bound *LpMIP* is the rearrangement of the loop connecting β -strands β 4 and
143 β 5 near the stalk helix. Ligand binding to *LpMIP* in solution was probed by titrating ^2H , ^{15}N -labeled
144 *LpMIP* with JK095 (Fig. 2B, C). Chemical shift perturbations were observed in the FKBP-like domain,
145 consistent with the binding site identified in the crystal structure. In addition, residues within the FKBP
146 domain facing the stalk helix, the stalk helix and the dimerization domain show chemical shift
147 perturbations upon JK095 binding. The amide resonances between residues ~57-76 in the N-terminal
148 half of the *LpMIP* stalk helix show severe line broadening and were thus not visible in the protein's ^1H ,
149 ^{15}N -HSQC NMR spectrum (Fig. 2C, Fig. S2A). This suggests motions in the μs -ms timescale in this
150 region. The FKBP-like domain shows complex shift changes upon JK095 addition, with some regions
151 showing line broadening and others line sharpening. While crystallographic B-factors are generally less
152 well suited to assess dynamic changes, overall, the changes in the presence of JK095 agree with the
153 observed chemical perturbations in the NMR titrations. While this analysis is limited since the resolution
154 of the two structures is incomparable, focusing on the changes of the distribution of individual B-values
155 within individual structures together with the NMR data suggest dynamic quenching by the ligand
156 throughout the protein (Fig. 2D, E).

157
158 To assess the structural dynamics of *LpMIP* both locally and on a global scale in solution, we combined
159 NMR relaxation studies with pulsed electron paramagnetic resonance (EPR) spectroscopy and small
160 angle X-ray scattering (SAXS) (Fig. 3, Fig. S3-S6). NMR relaxation experiments informing on fast, ps-
161 ns amide bond fluctuations and dynamics overlying the protein's global rotational dynamics show that
162 *LpMIP* is relatively rigid on the assessed timescale, except for the very N-terminus, the linker between
163 β 3a and β 3b, the linker between β 4 and β 5 and the C-terminus (Fig. S3). In contrast to the influence of
164 JK095 on the protein dynamics on slower timescales, as was apparent through the changes in line
165 broadening, fast backbone dynamics were not, or only marginally affected by the inhibitor.

166

167 The results from EPR spectroscopy and SAXS further provide evidence of the high flexibility of *LpMIP*
168 in solution (Fig. 3). *LpMIP* does not contain native cysteine residues. Thus, single cysteine mutants in
169 the middle of the stalk helix (*LpMIP* K80C) and at the C-terminal end of the FKBP-like domain (*LpMIP*
170 S208C) were introduced and labeled with nitroxide spin labels (Fig. 3A, Fig. S4, S5). Continuous wave
171 EPR confirmed a satisfactory labeling efficiency at both positions (Fig. 3B).

172 Pulsed EPR spectroscopy (pulsed electron-electron double resonance (PELDOR, also known as DEER))
173 was used to determine the distances between the two spin-labeled sites, and the measurements were
174 compared to simulations of the spin pair distance distributions based on the available crystal structures
175 (Fig. 3C-E, Table S2). The distance distributions obtained from spin labeled *LpMIP* K80C and S208C
176 were broader than expected from the crystal structures, indicating that these structures represent only a
177 subset of conformers in solution. Upon addition of JK095, no significant changes were observed for
178 *LpMIP* K80C, while for S208C the overall distribution shifted towards shorter distances. This could be
179 explained e.g., by structural changes of the two FKBP domains moving closer together. Of note, the
180 related NMR data show that at a molar protein:inhibitor ratio of 1:3 (n/n), the complex is already fully
181 saturated. The EPR measurements were carried out with a protein:inhibitor ratio of 1:5, indicating that
182 even when fully occupied, the “closed” conformation is only transiently populated.

183 Extensive structural dynamics of *LpMIP* in solution are also apparent from SEC-SAXS experiments
184 (Fig. 3F-K, Fig. S6, Table S3). Here, the *LpMIP* scattering profiles did not match a simulated scattering
185 curve using the available crystal structure, again suggesting a more complex conformational ensemble
186 in solution. For a better fit with the experimental SAXS data of *LpMIP* in solution, SREFLEX modeling
187 was carried out [37] and *LpMIP* structural models with straight and kinked stalk helices were obtained
188 (Fig. 3J, K). While there were no discernible differences between the *apo* and JK095-bound state in the
189 *LpMIP* SREFLEX models, which may reflect the loss of JK095 during size exclusion chromatography
190 (see below), the SAXS data show high domain flexibility concurrent with the EPR experiments.

191

192 **The appendage domains influence *LpMIP* dynamics and stability**

193 Due to their high expression yields and solubility, deletion rather than full-length constructs have
194 frequently been used for structural studies of both MIP and FKBP inhibitor complexes [21,38].
195 However, this may not only inadequately reflect the complexity of the therapeutic target, but also
196 compounds a lack of understanding how the appendage domains affect protein structural dynamics and
197 inhibitor binding. This question is exacerbated by our observation that ligand binding to the FKBP-like
198 domains is sensed throughout the entire protein (Fig. 2).

199 In combination with our structural and spectroscopic studies on full-length *LpMIP*, the modular
200 architecture of *LpMIP* provides a unique opportunity to explore such questions through deletion
201 mutants. To emulate the structural diversity of MIP proteins from other human-pathogenic microbes,
202 we generated two shortened *LpMIP* constructs, *LpMIP*⁷⁷⁻²¹³ and *LpMIP*¹⁰⁰⁻²¹³ (Fig. S7A). *LpMIP*⁷⁷⁻²¹³,

203 containing the FKBP-like domain and a bisected stalk helix thus resembling *T. cruzi* MIP [26], is the
204 construct typically used in *in vitro* ligand binding studies [20,21,39]. $LpMIP^{100-213}$, which consists solely
205 of the FKBP domain, resembles e.g. *B. pseudomallei* MIP [33]. Both $LpMIP^{77-213}$ and $LpMIP^{100-213}$ are
206 monomeric and structurally intact as seen by size exclusion chromatography (SEC) and circular
207 dichroism (CD) spectroscopy (Fig. S7B-D). In a fluorescence-based assay, we saw that the melting
208 temperature (T_m) depended greatly on the protein's appendage domains. (Fig. 4A). With 51.4 ± 0.3 °C,
209 the T_m of $LpMIP^{100-213}$ was found to be ~ 14 °C below that of the slightly longer construct $LpMIP^{77-213}$
210 (64.6 ± 0.6 °C) and ~ 9 °C lower than that of full-length $LpMIP$ (60.7 ± 0.3 °C) (Fig 4A top). In all three
211 constructs, addition of JK095 led to an increase in the melting temperature commensurate with protein
212 stabilization upon inhibitor binding (Fig. 4A bottom). However, this effect was less pronounced for
213 $LpMIP^{100-213}$ ($\Delta T_{m(JK095-apo)} = +2.8$ °C) compared to both longer constructs ($\Delta T_{m(JK095-apo)} = +3.8$ °C. This
214 may reflect the strongly reduced binding affinity of JK095 to $LpMIP^{100-213}$ ($K_d = 20.47 \pm 4.48$ μ M)
215 compared to $LpMIP^{77-213}$ ($K_d = 2.27 \pm 0.01$ μ M) and full-length $LpMIP$ ($K_d = 1.27 \pm 0.14$ μ M) (Fig. S1).
216 The differences in T_m and inhibitor binding affinity suggest that the appendage domains, in particular
217 the part of the stalk helix directly preceding the FKBP domain, play an important role in protein stability
218 and ligand binding.

219
220 To investigate the structural crosstalk between appendage and FKBP domains in $LpMIP$ in more detail,
221 we used NMR spectroscopy. With the backbone assignments of all three $LpMIP$ constructs in the *apo*
222 and JK095-bound states (Fig. S2), the chemical shifts for residues within the FKBP-like domains were
223 compared (Fig. 4C, D). In the absence of inhibitor, there were only minor differences between full-
224 length $LpMIP$ and $LpMIP^{77-213}$, except for the very N-terminal residues where the cleavage site is located
225 (Fig 4C top, orange). Interestingly, differences between the two constructs became slightly more
226 pronounced in the presence of JK095, particularly for residues 184 to 194 belonging to the $\beta 4/\beta 5$ loop
227 (Fig 4C bottom, orange).

228 In contrast, the comparison between full-length $LpMIP$ with $LpMIP^{100-213}$ already showed strong
229 chemical shift perturbations in the *apo* state (Fig 4C top, cyan). Most notable were the effects in the
230 vicinity of residue 160 within the canonical ligand binding site, and between residues 180 and 200,
231 which are part of the long loop between β -strands 4 and 5 and form an interaction network with the C-
232 terminal half of the stalk helix (Fig. 4D, E). Furthermore, in the 1H , ^{15}N -HSQC spectrum of $LpMIP^{100-}$
233 213 , no or extremely weak resonances for S115-N117, K146/T147, I159 and R188 were observed, while
234 these were clearly visible in both longer constructs (Fig. 4D, E, Fig. S2). This suggests that these regions
235 show altered dynamics in the absence of the stalk helix. However, except for residue I159 as well as
236 R188 in the $\beta 4/5$ loop, none of these residues are directly involved in FKBP/stalk helix interactions or
237 part of the canonical ligand binding site, thus suggesting allosteric effects on the canonical binding site
238 through the stalk helix. Potentially, such long-range crosstalk could be mediated through a hydrophobic
239 interaction network between the stalk helix and FKBP-like domain (Fig. 4E).

240 Since the residues across all three full-length *LpMIP* domains showed no significant differences in their
241 respective backbone dynamics in the ps-ns timescale in $\{^1\text{H}\}^{15}\text{N}$ -hetNOE experiments between the *apo*
242 and the JK095-bound states (Fig. S3A), stalk helix removal seems to mostly affect slower, μs -ms
243 motions within the FKBP-like domain. In the absence of the stalk helix, marginally increased hetNOE
244 values for *LpMIP*⁷⁷⁻²¹³ and *LpMIP*¹⁰⁰⁻²¹³ could indicate slightly subdued backbone dynamics of the
245 FKBP-like domain within the loops connecting $\beta 3\text{a}/\beta 3\text{b}$ and $\beta 4/\beta 5$, both in the absence and presence of
246 JK095 (Fig. S3B,C).

247

248 **Role of the appendage domains for FKBP-like domain inhibitor binding**

249 To gauge a possible structural role of the appendage domains for ligand binding in *LpMIP* as suggested
250 by our thermostability assays and NMR data (Fig. 4), we determined the crystal structures of *LpMIP*⁷⁷⁻
251 ²¹³ (PDB: 8BK5) and *LpMIP*¹⁰⁰⁻²¹³ (PDB: 8BK6) with JK095 at 2.26 and 1.49 Å resolution, respectively
252 (Fig. 5A). These complement the crystal structure of full-length *LpMIP* with JK095 (PDB: 8BJD, Fig.
253 2). The largest structural differences across all three *LpMIP* constructs are observed in the $\beta 4/\beta 5$ loop,
254 while the side chains of the active site residues adopted nearly identical orientations. JK095 bound to
255 *LpMIP*⁷⁷⁻²¹³ adopted a very similar binding stance as seen in the canonical binding pocket of full-length
256 *LpMIP* (Fig. 5A, B). However, in *LpMIP*⁷⁷⁻²¹³, the inhibitor's hydroxymethyl group adopted two
257 orientations while in full-length *LpMIP*, only the orientation facing away from the sidechain of D142
258 was observed, thereby forgoing the formation of a possible hydrogen bond interaction. Furthermore, the
259 pyridine ring nitrogen was 2.7 Å away from the Y185 sidechain hydroxyl group in *LpMIP*⁷⁷⁻²¹³, while
260 this distance increased to 3.7 Å in full-length *LpMIP*.

261 In contrast to the two longer constructs, the inhibitor binding site in *LpMIP*¹⁰⁰⁻²¹³ was not clearly defined
262 in the crystal structure (Fig. S8). To verify the possibility of drastically altered ligand interaction to the
263 FKBP-like domain in the absence of the appendage domains in solution, we compared the chemical shift
264 perturbations of the three ¹⁵N-labeled *LpMIP* constructs titrated with JK095 (Fig. 5B-E, Fig. S2A-C).
265 As expected, the chemical shift changes in full-length *LpMIP* and *LpMIP*⁷⁷⁻²¹³ agree with the binding
266 site observed in the respective complex crystal structures. In stark contrast, addition of JK095 to
267 *LpMIP*¹⁰⁰⁻²¹³ affected a significantly larger number of residues and the chemical shift perturbation pattern
268 was not restricted to the canonical ligand binding site. Of note, *LpMIP*¹⁰⁰⁻²¹³ crystallized as a parallel
269 dimer with the loop between $\beta 4$ and $\beta 5$ mediating many of the dimer contacts (PDB: 8BK6, Fig S8).
270 These loops showed the largest structural differences between the two *LpMIP*¹⁰⁰⁻²¹³ protomers in the unit
271 cell and the largest chemical shift changes upon addition of JK095 in the NMR experiments. We thus
272 wondered whether transient oligomerization could be responsible for the extensive JK095-dependent
273 chemical shift perturbations in the 12 kDa *LpMIP*¹⁰⁰⁻²¹³ construct. Under the assumption of isotropic
274 tumbling, a rotation correlation time τ_c of 5.6 ns can be approximated according to the Stokes-Einstein
275 equation for a spherical globular, monomeric protein of that size at 25 °C (see material and methods for
276 details). By applying an empirical formula [40], a τ_c value of 7.3 ns can be derived for a 12 kDa

277 molecule. Accordingly, neither the overall narrow line widths in the NMR spectra of ^{15}N -labeled
278 $LpMIP^{100-213}$ (Fig. S2C), nor the experimentally determined rotation correlation times ($\tau_c = 6.8 \pm 0.9$ ns
279 for the *apo* protein, $\tau_c = 6.4 \pm 0.7$ ns in the presence of JK095) are indicative of inhibitor-induced dimer
280 formation of $LpMIP^{100-213}$. Rather, the extensive NMR chemical shift perturbations in $LpMIP^{100-213}$ upon
281 addition of JK095 are likely caused by the non-specific interaction with the inhibitor. This finding
282 supports the notion that the $LpMIP$ appendage domains, particularly the C-terminal half of the stalk
283 helix, play a decisive role in ligand binding to and dynamics within the FKBP domain.

284

285 **Comparison of $LpMIP$ and human FKBP51 in complex with the same [4.3.1]-aza-bicyclic** 286 **sulfonamide inhibitor**

287 $LpMIP^{77-213}$ shares 32 % sequence similarity with a construct of human FKBP51 (residues 16-140) that
288 was recently co-crystallized with JK095 [41]. The two complex crystal structures (PDB IDs: 5OBK,
289 8BK5) align with a backbone RMSD of 0.776 Å (Fig. 6A). All residues interacting with JK095 are
290 conserved between the two proteins (Fig. 6B). A conserved tyrosine residue (Y113/Y185 in
291 FKBP51/ $LpMIP$) responsible for forming a H-bond to the nitrogen of the pyridine or bicycle of the
292 inhibitor adopted the same orientation in both proteins. The sidechain of residue 159 forms a
293 hydrophobic lid below the bi-cycle by forming van der Waals contacts with the inhibitor's bi-cycle
294 carboxy group. In addition, a barrage of aromatic residues in either protein nestles the bi-cyclic inhibitor
295 core from below (Fig. 6B).

296 The inhibitor's pyridine group, bi-cyclic core and sulfonamide group align well between the two
297 proteins, only the di-chlorophenyl moiety is slightly differently tilted. Slight structural variations in the
298 $\beta 3a$ -strand within the FKBP domain were found between FKBP51 and $LpMIP$, namely across residues
299 $^{67}\text{FDS}^{69}$ and $^{141}\text{FDS}^{143}$, respectively. The aromatic residue in this stretch may stabilize the di-
300 chlorophenyl moiety through T-shaped π stacking. Inhibitor binding may also be affected by the
301 structural and sequential differences in the loop connecting $\beta 4$ and $\beta 5$ ($^{117}\text{GSLPKI}^{122}$ in FKBP51 and
302 $^{189}\text{SVGGPI}^{194}$ in $LpMIP$). Sitting on top of the di-chlorophenyl moiety of the ligand, the respective
303 isoleucine residue within this stretch, together with the abovementioned phenylalanine in $\beta 3a$, form a
304 hydrophobic platform against which the di-chlorophenyl ring rests. In the case of FKBP51, the sidechain
305 of S118 may additionally contact one chloro-substituent and thereby help to orient it. In contrast, the
306 loop orientation observed in the $LpMIP^{77-213}$ crystal structure may disfavor interactions of either of the
307 two chlorine groups with loop sidechains. The structural perturbation of the $^{67/141}\text{FDS}^{69/143}$ motif in the
308 $\beta 3a$ -strand also led to slightly different orientations of its central aspartic acid sidechain when comparing
309 the structures of FKBP51 $^{16-140}$ and $LpMIP^{77-213}$. In both cases, the bound JK095 ligand's hydroxymethyl
310 group adopts two orientations. However, in FKBP51 $^{16-140}$, neither orientation comes close enough to
311 form a hydrogen bond with the aspartic acid side chain of D68 (O-O distance 4.0 Å). In contrast, in
312 $LpMIP^{77-213}$, in one of the two orientations the distance to the corresponding residue D142 is reduced by

313 0.9 Å compared to FKBP51¹⁶⁻¹⁴⁰. In the other orientation, the inhibitor hydroxyl group can form
314 hydrogen bonds with water molecules (~~see below~~).

315

316 **Methylation leads to improved inhibitor binding to MIPs from different pathogenic** 317 **microorganisms**

318 It was recently observed that the stereospecific introduction of a methyl group at the C_α position of the
319 pyridine substituent of bicyclic [4.3.1]-aza-amide inhibitors significantly increased their affinity for
320 FKBP51 due to displacement of a surface water molecule [41]. JK095 does not carry such a methyl
321 group and in our complex structure with *LpMIP*⁷⁷⁻²¹³, we observed a crystallographic water in a similar
322 surface position as the one that originally inspired the inhibitor methylation studies for human FKBP51
323 [41] (Fig. 7A). We thus wondered whether inhibitor methylation may be used to improve the affinity of
324 bicyclic sulfonamides for MIP proteins from pathogenic microorganisms. To test this hypothesis, we
325 introduced a methyl group into JK095, yielding JK236 (Scheme 1) and determined the co-crystal
326 structure of *LpMIP*⁷⁷⁻²¹³ with JK236 at 1.49 Å resolution (PDB: 8BJE) (Fig. 7B-D).

327 Overall, the structures of *LpMIP*⁷⁷⁻²¹³ with JK095 and JK236 align with an RMSD of 0.283 Å and show
328 no notable differences in protein sidechain or inhibitor conformations. Together with NMR chemical
329 shift perturbation data of ¹⁵N-labeled *LpMIP*⁷⁷⁻²¹³ titrated with JK095 or JK236 (Fig. 7E, F, Fig. S2D),
330 this confirmed that both ligands interact in a highly similar fashion with the *LpMIP* FKBP-like domain.
331 Furthermore, pulsed EPR measurements of spin-labeled full-length *LpMIP* K80C and *LpMIP* S208C
332 showed that JK236 affects the structural ensemble of full-length *LpMIP* in a similar manner as JK095
333 (Fig. 7G, Fig. S5, S6).

334 Nonetheless, the binding affinity of JK236 to *LpMIP*⁷⁷⁻²¹³ and full-length *LpMIP* was increased by
335 roughly one order of magnitude for the methylated ($K_d = 123.5 \pm 47.4$ nM and 108.5 ± 10.6 nM),
336 compared to the unmethylated compound (2.27 ± 0.01 μM and 1.27 ± 0.14 μM) (Fig. S1). Presumably
337 reflecting the increased affinity of JK236 over JK095, the SAXS data also show a more pronounced
338 reduction in R_g and D_{max} for full-length *LpMIP* in the presence of the methylated inhibitor (Fig. 7H-J).
339 Despite the presence of a less defined inhibitor interaction site in *LpMIP*¹⁰⁰⁻²¹³, an increase in affinity
340 was also observed for the shortest *LpMIP* construct for the methylated ligand ($K_d = 20.47 \pm 4.48$ μM vs
341 1.31 ± 0.24 μM for JK095 and JK236, respectively).

342 A surface water molecule is indeed displaced in the JK236 co-crystal structure compared to the complex
343 with JK095 (Fig. 7A). While the two inhibitors bound to *LpMIP* superimpose nearly perfectly, the
344 orientation of the hydroxymethyl group is fixed in JK236 in contrast to the two orientations observed
345 for JK095. In JK236, the hydroxymethyl group faces away from the sidechain of D142 and instead
346 exclusively forms a hydrogen bridge with a water molecule. At a resolution of 1.49 Å, the additional
347 methyl group in JK236 can also be placed unambiguously in the crystal structure and is seen to point
348 into the solvent where it does not undergo any protein contacts but rather displaces a water molecule
349 (Fig. 7A). This shows that the methylation of bicyclic ligands to obtain high-affinity binders through

350 surface water displacement is feasible for *Lp*MIP and may constitute a general concept for FKBP as
351 well as microbial MIPs.

352

353 To gauge whether methylation for improved binding is indeed applicable to MIPs from other human
354 pathogens including those of eukaryotic origin, we turned to the protozoan *Trypanosoma cruzi*, the
355 causative agent of Chagas disease. With a free-standing stalk helix and a prototypical FKBP domain,
356 the *T. cruzi* MIP protein (*Tc*MIP) structurally resembles the *Lp*MIP⁷⁷⁻²¹³ construct lacking the
357 dimerization domain and N-terminal half of the stalk helix (Fig. 8).

358 Similar to *Lp*MIP, ligand binding to *Tc*MIP was improved for the methylated ($K_d = 45.5 \pm 9.2$ nM)
359 versus the non-methylated compound (599.0 ± 25.5 nM) (Fig. S1). Our crystal structure of *Tc*MIP in
360 complex with JK236 (PDB: 8BK4) at 1.34 Å resolution confirms the interaction of JK236 with the
361 canonical binding site in the FKBP-like domain and a highly similar interaction mode as seen for *Lp*MIP
362 (Fig. 8, Fig. S9).

363 The complex structure aligns to the previously published structure of *apo Tc*MIP (PDB: 1JVW) [26]
364 with an RMSD of 0.499 Å (Fig. 8A). The largest differences between the two proteins are seen again in
365 the loop connecting β-strands 4 and 5, as well as in β-strand 3a. In the *Tc*MIP *apo* structure, multiple
366 water molecules are found around the substrate binding site which are absent with JK236, but no surface
367 water molecule is seen in the same position as detected in JK095-bound FKBP51 [34] and *Lp*MIP.
368 However, due to the lack of a complex structure of *Tc*MIP with JK095, it is difficult to assess the
369 consequences of inhibitor methylation on water occupancy in *Tc*MIP in detail. Nonetheless, the similar
370 gain in binding affinity through the introduction of the methyl group into the bi-cyclic inhibitor indicates
371 a similar mode of action that can be exploited for the development of high-affinity binders against MIP
372 proteins from various pathogens. The availability of two structures of MIP proteins from highly diverse
373 pathogenic microorganisms in complex with the same synthetic inhibitor now also provides a unique
374 opportunity to elucidate the possibility to generate pan-inhibitors.

375

376 Discussion

377 The role of MIPs as widespread microbial virulence factors has spurred efforts to develop inhibitors
378 targeting the MIP FKBP-like domain as the most conserved MIP domain. However, many MIP proteins
379 contain additional appendage domains of unknown function. This prompted us to investigate the
380 interdomain crosstalk and dynamics of the homodimeric *Legionella pneumophila* MIP protein as a
381 representative model system for multi-domain MIPs in more detail.

382 Intrinsic structural flexibility seems to be a hallmark of homodimeric MIP proteins from pathogenic
383 microorganisms [42]. Not only did we notice significant stalk helix splaying between the two available
384 crystal structures of full-length *Lp*MIP in the absence of a ligand, but a recently published structure of
385 unliganded, homodimeric *P. aeruginosa* FkbA, which shares the same three-domain architecture,
386 showed both straight and bent stalk helices in the crystal structure [25]. It has been suggested that

387 variations in crystal structures are a good proxy for dynamics in solution [43] and in the case of *LpMIP*,
388 we can support and extend this notion with EPR and NMR spectroscopy as well as SAXS. Our crystal
389 structures provide a glimpse of the protein's dynamics, but the full extent of its domain gymnastics in
390 solution required a multi-faceted approach.

391 Using NMR spectroscopy, we identified a dynamic hotspot in the central stalk helix of *LpMIP*. This is
392 also the region that shows extensive kinking in our SAXS SREFLEX models. A difference in "bending"
393 of the central stalk helix was mentioned previously for a co-crystal of full-length *LpMIP* with FK506
394 [14], although the corresponding data set has never been submitted to the PDB and thus cannot be
395 analyzed in detail here. Pervushin and colleagues reported that the *E. coli* FkpA stalk helix rigidifies in
396 the presence of a client protein and led to reduced interdomain mobility [42]. Here, we saw that binding
397 of a bi-cyclic vinylsulfone inhibitor led to complex changes throughout the protein, possibly including
398 the rigidification of the N-terminal half of the stalk helix.

399 Comparing JK095-bound *LpMIP*⁷⁷⁻²¹³ with the rapamycin-bound protein (Fig. S10), shows the relative
400 displacement of the ligand enclosing sidechains and indicates that the active site of *LpMIP* displays a
401 conformational flexibility commensurate with its ability to bind to differently sized ligands. Across all
402 our structures, the $\beta 4/\beta 5$ loop, which interacts with the stalk helix and may thus serve as a substrate-
403 selective communication node between stalk and FKBP-like domain, showed the most structural
404 variations. In contrast to previous observations with rapamycin [21], no significant rigidification of
405 FKBP-like domain loops on very fast timescales was observed with JK095, while slower dynamics were
406 quenched throughout the protein upon ligand binding. Different inhibitor molecules could thus
407 potentially mimic the structural and dynamic consequences of diverse, yet unidentified, native ligands.
408 Unfortunately, the affinity of collagen peptides, the only known native *LpMIP* substrate to date [19,20],
409 is too low for detailed structural and dynamic analysis.

410 Furthermore, the addition of bi-cyclic inhibitors led to a population shift but not a full transition to a
411 "closed" conformation with decreased distances between the FKBP-like domains in our EPR
412 experiments. Whether this is a general feature of *LpMIP* ligands or unique to the tested inhibitors is
413 unknown. Future ligand screening could explore whether the ability of ligands to shift the *LpMIP*
414 conformational ensemble to a closed state correlates with its antimicrobial efficiency.

415 We could also show that the *LpMIP* domains engage in bidirectional crosstalk. Ligand binding at the
416 FKBP-like domain affected the stalk helix and dimerization domain, and, in turn, stalk helix deletion
417 reduced protein stability and, surprisingly, led to the loss of a defined ligand binding mode. The
418 allosteric modulation of ligand binding by the C-terminal half of the stalk helix has interesting
419 implications for ligand recognition and regulation of MIP proteins from other pathogenic species, such
420 as *Burkholderia pseudomallei*, which naturally lack a stalk helix and dimerization domain [33].

421 Deletion constructs of MIP proteins have been commonly used to study inhibitor binding. Our data
422 suggests that a construct retaining the C-terminal half of the stalk helix is suitable for most applications,
423 but there are nonetheless some differences to consider. The increased melting temperature of *LpMIP*⁷⁷⁻
424 ²¹³ may indicate that stabilization of the FKBP domain by the stalk helix' C-terminal end is counteracted
425 by the protein's flexibility in the N-terminal half. Complete deletion of the stalk helix has negative
426 consequences for both protein stability and ligand interactions.

427 Bi-cyclic sulfonamides have antiproliferative effects against *L. pneumophila* and *Chlamydia*
428 *pneumoniae*, which both express MIP proteins [34]. This suggests that the bicyclic sulfonamide scaffold
429 is a promising starting point for drug development. Our results on *T. cruzi* MIP suggest that both
430 prokaryotic and eukaryotic MIP proteins can be targeted with a high-affinity pan-inhibitor, and lessons
431 from human FKBP's such as site-specific methylation [41] can be exploited to improve inhibitor affinity
432 for microbial MIPs. However, the structural similarities between MIPs and FKBP's pose challenges,
433 particularly since FKBP inhibition leads to immunosuppression, the opposite of the desired effect in
434 fighting severe infections. Here, we could carry out a structural comparison of a microbial MIP with a
435 human FKBP in complex with the same synthetic ligand for the first time. In a previous NMR study on
436 FKBP51, the central aromatic residue in the β 3a-strand, was seen to flip in and out of the binding pocket,
437 a process important for ligand selectivity [44]. The residues stabilizing the "outward" position (FKBP51
438 K58, K60 and F129) are not fully conserved in *LpMIP* (T132, R134, F202). Hence ring flipping might
439 be an important distinguishing feature between the two proteins. Additional structures and dynamic
440 studies of human FKBP's and microbial MIPs in complex with the same ligands, possibly with other
441 molecular scaffold architectures, may be helpful in making further progress in this area.

442 In summary, we found that in *Legionella pneumophila* MIP, the stalk helix decisively modulates ligand-
443 binding behavior of the FKBP-like domain, the most conserved domain across all MIP proteins. This,
444 together with the high intrinsic flexibility of MIP proteins and the ability to engage with structurally
445 diverse ligands, suggests that MIP appendage domains can be used to fine-tune substrate responses and
446 suggest they play a contextual role in the survival and replication of pathogenic microorganisms.

447

448 **Material and Methods**

449 **Cloning, protein expression and purification**

450 Genes coding for *Legionella pneumophila* LpMIP¹⁻²¹³, LpMIP⁷⁷⁻²¹³, LpMIP¹⁰⁰⁻²¹³ and *Trypanosoma cruzi*
451 TcMIP with a His₆-tag were obtained from GenScript (Piscataway Township, NJ, USA) and cloned into
452 a pET11a vector. Single cysteine mutants for EPR spectroscopy were introduced at positions K80C and
453 S208C in LpMIP¹⁻²¹³ via site directed mutagenesis using the following primer pairs:

454 K80C forward: 5'-CCGCGGAGTTTAACAAGTGCGCGGATGAAAACAAGG-3'

455 K80C reverse 5'- ACCTTGTTTTTCATCCGCGCACTTGTTAAACTCCGCG-3'

456 S208C forward 5'- TAAGATTCACCTGATCTGCGTGAAGAAAAGCAG - 3'

457 S208C reverse 5'- CTGCTTTTCTTCACGCAGATCAGGTGAATCTTA - 3

458 Freshly transformed *E. coli*. BL21 gold (DE3) cells were grown at 37 °C to an OD₆₀₀ of 0.6 and then
459 induced with 1 mM IPTG and grown overnight at 20 °C. ²H, ¹⁵N-labeled LpMIP¹⁻²¹³ was obtained by
460 growing cells in commercially available Silantes OD2 *E. coli* medium (Silantes GmbH, Munich,
461 Germany). ¹³C, ¹⁵N-labeled LpMIP⁷⁷⁻²¹³ and LpMIP¹⁰⁰⁻²¹³ were obtained by growing cells in minimal
462 medium with ¹⁵N-NH₄Cl and ¹³C-glucose as the sole nitrogen and carbon sources. Cells were harvested
463 by centrifugation (5000×g, 10 min, 4 °C). The cell pellet was frozen in liquid nitrogen and stored at
464 - 20 °C until further use.

465 For purification of LpMIP¹⁻²¹³ and LpMIP⁷⁷⁻²¹³, the cell pellet was dissolved in lysis buffer (20 mM Tris
466 pH 8, 20 mM Imidazole pH 8, 300 mM NaCl, 0.1 % Tx100, 1 mM DTT, 1 mM benzamidine, 1 mM
467 PMSF, DNase, RNase and lysozyme). Cells were disrupted passing them three times through a
468 microfluidizer (Maximator) at 18,000 psi. Membranes and cell debris were pelleted at 48,380xg, 30 min,
469 4 °C and the supernatant was loaded onto a NiNTA column (Qiagen, Hilden, Germany) previously
470 equilibrated with washing buffer (20 mM Tris pH 8, 300 mM NaCl and 20 mM imidazole). After
471 washing with 10 CV (column volumes) of washing buffer, the protein of interest was eluted with 5 CV
472 of elution buffer (20 mM Tris pH 8, 300 mM NaCl and 500 mM imidazole pH 8). Proteins were dialyzed
473 overnight at 4 °C in 20 mM Tris pH 8, 300 mM NaCl in the presence of His-tagged TEV protease (1:20
474 mol/mol) to cleave the His-tag from the MIP constructs.
475 Dialyzed protein was then loaded onto a fresh NiNTA column. The flow through was collected and the
476 column was washed with 4 CV of washing buffer to obtain the maximum amount of tag-free MIP
477 protein. For the purification of LpMIP¹⁰⁰⁻²¹³ the same protocol was applied, with all buffers adjusted to
478 pH 7. After concentration, the proteins were loaded on a size exclusion column (HiLoad 16/600
479 Superdex 200 pg, Cytiva, Freiburg, Germany) equilibrated with size exclusion buffer (20 mM Tris pH 7,
480 150 mM NaCl for LpMIP⁷⁷⁻²¹³ and LpMIP¹⁰⁰⁻²¹³ and 50 mM Tris pH 7, 150 mM NaCl for LpMIP¹⁻²¹³).
481 The fractions containing pure protein were pooled and sample purity was verified by SDS-PAGE.

482

483 **Crystallization, data collection and structure determination of LpMIP inhibitor complexes**

484 Following size exclusion chromatography, each of the proteins were kept in a solution of 20 mM Tris
485 and 150 mM NaCl at pH 7.0 and were concentrated to 10 mg/mL using a 10,000 MWCO concentrator.
486 Each protein was mixed with the crystallization buffer in a ratio of 2:1, and, where appropriate, with a
487 1:5 molar ratio of inhibitor. Inhibitors were synthesized as previously described [34,41]. All crystals
488 were obtained using sitting drop *vapor* diffusion via custom screens with the following conditions:
489 *LpMIP*¹⁻²¹³ 20 % (w/v) PEG 6000, 500 mM zinc acetate dihydrate, 100 mM MES, pH 6.0. *LpMIP*¹⁻
490 ²¹³JK095 15 % (w/v) PEG 6000, 500 mM zinc acetate dihydrate, 100 mM MES, pH 6.5. *LpMIP*¹⁰⁰⁻²¹³
491 JK095 20 % (w/v) PEG 8000, 500 mM zinc acetate dihydrate, 100 mM MES, pH 5.8. *LpMIP*⁷⁷⁻²¹³ JK095
492 20 % (v/v) 2-propanol, 0.2 M sodium citrate tribasic dihydrate, 0.1 M HEPES, pH 7.5. *LpMIP*⁷⁷⁻²¹³
493 JK236 18 % (w/v) PEG 8000, 0.2 M zinc acetate, 0.1 M sodium cacodylate, pH 6.5. *TcMIP* JK236
494 30 % (v/v) MPD, 0.2 M ammonium acetate, 0.1 M sodium citrate, pH 5.6. Crystals were briefly soaked
495 in 30 % (v/v) glycerol for cryo-protection and subsequently flash-frozen in liquid nitrogen in preparation
496 for diffraction experiments at synchrotron energy. Data were collected at beam line ID23-1 and ID30A-
497 3 (ESRF, Grenoble).

498 Crystals of the MIP series diffracted between 1.3 and 2.4 Å resolution (Table 1). Data were processed
499 with XDS [45] and structures were solved by Molecular Replacement with Phaser [46] using previously
500 published models of MIPs (PDB ID: 1FD9, 1JVW). Manual rebuilding was performed with COOT [47]
501 and refinement with Refmac [48]. The refined models were deposited into the PDB repository with the
502 following IDs: 8BJC, 8BJD, 8BJE, 8BK4, 8BK5, 8BK6. Images were prepared using Pymol
503 (Schrödinger, LLC), CorelDRAW (Corel), UCSF ChimeraX [49] and Blender (Blender Foundation).

504

505 **Analytical Size-exclusion chromatography (SEC)**

506 20 µM of purified *LpMIP* constructs (*LpMIP*¹⁻²¹³, *LpMIP*⁷⁷⁻²¹³ or *LpMIP*¹⁰⁰⁻²¹³) in 20 mM Tris pH 7,
507 150 mM NaCl were used. For the *apo* state protein, a final concentration 0.02 % DMSO was added. A
508 5-fold molar excess of JK095 in DMSO was added (0.02 % final DMSO concentration). Samples were
509 injected on a Superdex200 Increase 10/300 GL (Cytiva) column via an NGC chromatography system
510 (BioRad).

511

512 **Circular Dichroism (CD) spectroscopy**

513 CD measurements were conducted on a Jasco J-1500 CD spectrometer (Jasco, Gross-Umstadt,
514 Germany) with 1 mm quartz cuvettes using 3.5 µM protein in 5 mM Tris pH 7 and 2.5 mM NaCl.
515 Spectra were recorded at 25 °C in a spectral range between 190 – 260 nm with 1 nm scanning intervals,
516 1.00 nm bandwidth and 50 nm/min scanning speed. All spectra were obtained from the automatic
517 averaging of five measurements.

518

519 **Isothermal Titration Calorimetry (ITC)**

520 Experiments were performed in an isothermal titration calorimeter (Microcal ITC200 - Malvern
521 Panalytical) at 25 °C with a reference power of 11 μ Cal/sec, an initial delay of 120 seconds and a stirring
522 speed of 750 rpm. Protein concentration within the cell was between 20 and 40 μ M and ligand
523 concentration in the syringe was between 0.5 and 1 mM. Protein and inhibitors (JK095 and JK236) were
524 prepared in 20 mM Tris pH 8, NaCl 150 mM and 5 % DMSO. For each titration, 20 injections (spacing
525 between injections was 180 sec, duration was 0.4 sec) of 2 μ L inhibitor solution were carried out. The
526 curves were fitted using Origin.

527

528 NMR spectroscopy

529 All NMR spectra were obtained at 298.2 K on 600 MHz Bruker AvanceIII HD or Neo NMR
530 spectrometer systems equipped with 5-mm triple resonance cryo-probes. The spectrometers were locked
531 on D₂O. The ¹H chemical shifts of the ²H, ¹⁵N-labelled *LpMIP*¹⁻²¹³, ¹³C, ¹⁵N-labelled *LpMIP*⁷⁷⁻²¹³ and ¹³C,
532 ¹⁵N-labelled *LpMIP*¹⁰⁰⁻²¹³ were directly referenced to 3-(trimethylsilyl)propane-1-sulfonate (DSS). ¹³C
533 and ¹⁵N chemical shifts were referenced indirectly to the ¹H DSS standard by the magnetogyric ratio
534 [50]. *LpMIP*¹⁻²¹³ was measured in 50 mM Tris HCl pH 7, 150 mM NaCl, 0.1 mM DSS, 0.05 % NaN₃
535 and 10 % D₂O. Sample conditions for *LpMIP*⁷⁷⁻²¹³ and *LpMIP*¹⁰⁰⁻²¹³ were the same except 20 mM
536 Tris HCl pH 7 was used. Final protein concentrations were in the range of 100-150 μ M. All spectra were
537 processed using Bruker Topspin 4.1.1 and analyzed using CcpNmr Analysis [51] v2.5 (within the
538 NMRbox virtual environment [52]).

539 The previously published NMR backbone assignments of *LpMIP*¹⁻²¹³ (BMRB entry 7021) and *LpMIP*⁷⁷⁻
540 ²¹³ (BMRB entry 6334)^{37,38} were transferred to our spectra and verified using band-selective excitation
541 short-transient (BEST) transverse relaxation-optimized spectroscopy (TROSY)-based HNCA or
542 HNCACB experiments under our buffer conditions. In contrast, the assignment of *LpMIP*¹⁰⁰⁻²¹³ had to
543 be determined *de novo* by a set of BEST-TROSY-based HN(CA)CO, HNCA and HN(CO)CA, as the
544 ¹H, ¹⁵N-HSCQ spectrum of this construct differed significantly from the resonances of the FKBP domain
545 in both *LpMIP*⁷⁷⁻²¹³ and full-length *LpMIP*.

546 Standard NMR pulse sequences implemented in Bruker Topspin library were employed to obtain R_1 , R_2
547 and ¹⁵N,{¹H}-NOE values. For *LpMIP*¹⁻²¹³, TROSY-sampling pulse sequences were used to ensure high
548 data quality. Longitudinal and transverse ¹⁵N relaxation rates (R_1 and R_2) of the ¹⁵N-¹H bond vectors of
549 backbone amide groups were extracted from signal intensities (I) by a single exponential fit according
550 to equation 1:

$$551 \quad I = I_0 e^{-(tR_{1/2})} \quad (1)$$

552 In R_1 relaxation experiments the variable relaxation delay t was set to 1000 ms, 20 ms, 1500 ms, 60 ms,
553 3000 ms, 100 ms, 800 ms, 200 ms, 40 ms, 400 ms, 80 ms and 600 ms. In all R_2 relaxation experiments
554 the variable loop count was set to 36, 15, 2, 12, 4, 22, 8, 28, 6, 10, 1 and 18. The length of one loop
555 count was 16.96 ms. In the TROSY-based R_2 experiments the loop count length was 8.48 ms. The

556 variable relaxation delay t in R_2 experiments is calculated by length of one loop count times the number
557 of loop counts. The inter-scan delay for the R_1 and R_2 experiments was set to 4 s.

558 The $^{15}\text{N}\{-^1\text{H}\}$ steady-state nuclear Overhauser effect measurements ($^{15}\text{N}\{^1\text{H}\}\text{-NOE}$) were obtained from
559 separate 2D $^1\text{H}\text{-}^{15}\text{N}$ spectra acquired with and without continuous ^1H saturation, respectively. The
560 $^{15}\text{N}\{^1\text{H}\}\text{-NOE}$ values were determined by taking the ratio of peak volumes from the two spectra,
561 $^{15}\text{N}\{^1\text{H}\}\text{-NOE} = I_{\text{sat}}/I_0$, where I_{sat} and I_0 are the peak intensities with and without ^1H saturation. The
562 saturation period was approximately $5/R_1$ of the amide protons.

563

564 The averaged ^1H and ^{15}N weighted chemical shift perturbations (CSP) observed in ^1H , ^{15}N -HSQC
565 spectra were calculated according to equation 2 [53]:

566
$$\text{CSP} = \sqrt{0.5 * [\Delta\delta_{\text{H}}^2 + (0.15 * \Delta\delta_{\text{N}})^2]} \quad (2)$$

567 Here, $\Delta\delta_{\text{H}}$ is the ^1H chemical shift difference, $\Delta\delta_{\text{N}}$ is the ^{15}N chemical shift difference, and CSP is the
568 averaged ^1H and ^{15}N weighted chemical shift difference in ppm.

569

570 The oligomerization state of a protein can be estimated from the rotational correlation time (τ_c), the time
571 it takes the protein to rotate by one radian under Brownian rotation diffusion. Under the assumption of
572 a spherical globular protein and isotropic motion, τ_c (in ns) can be roughly approximated from the
573 Stokes-Einstein equation (3):

574
$$\tau_c = \frac{4\pi\eta r_{\text{eff}}^3}{3k_{\text{B}}T} \quad (3)$$

575 where η is viscosity (0.89 mPa*s for water at 298.2 K), k_{B} the Boltzmann constant and T the absolute
576 temperature. The effective hydrodynamic radius r_{eff} can directly be correlated with molecular weight
577 (M_w):

578
$$r_{\text{eff}} = \sqrt[3]{\frac{3M_w}{4\pi\rho N_A}} + r_h \quad (4)$$

579 where ρ is the average protein density (1.37 g/cm³) and N_A the Avogadro constant. For our calculations
580 we used hydration layer radius of 3.2 Å.

581 Based on studies from the Northeast Structural Genomics Consortium an empirical formula could be
582 derived for direct correlation of M_w (in Da) and τ_c (in ns) for proteins in the range of 5-25 kD [40]:

583
$$\tau_c = 0.00062 * M_w - 0.15 \quad (5)$$

584 The rotational correlation time is directly accessible from the ratio of ^{15}N R_1 and R_2 relaxation rates of
585 backbone amide measured at a ^{15}N resonance frequency (ν_{N}) assuming slow isotropic overall motion
586 [40,54] (equation 6):

587
$$\tau_c = \frac{1}{4\pi\nu_{\text{N}}} \sqrt{\frac{6R_2}{R_1} - 7} \quad (6)$$

588 **Electron Paramagnetic Resonance (EPR) spectroscopy sample preparation**

589 For spin labelling, Ni-NTA-column-bound single cysteine mutants of *LpMIP*¹⁻²¹³ were incubated
590 overnight at 4 °C using a 15-fold excess of 3-(2-Iodoacetamido)-2,2,5,5-tetramethyl-1-pyrrolidinyloxy
591 (IPSL) after the washing steps and then purified as described above. Following the IPSL-labelling
592 procedure, 4 µL of D₈-glycerol or water was added to a 12 µL of *LpMIP* sample, mixed thoroughly and
593 gently transferred into a sample tube. The samples for continuous wave EPR were directly measured in
594 a 25 µL micropipettes (BRAND, Germany) with a 0.64-mm diameter at room temperature. Samples for
595 pulsed EPR were flash frozen in liquid nitrogen in a 1.6 mm quartz EPR tube (Suprasil, Wilmad
596 LabGlass) and stored at -80°C.

597

598 **Continuous-wave EPR measurements**

599 Continuous-wave (CW) EPR measurements were performed at X-band frequency (9.4 GHz) on a Bruker
600 EMXnano Benchtop Spectrometer at room temperature in a 25 µL micropipette (BRAND, Germany)
601 with a 0.64 mm diameter. The spectra were acquired with 100 kHz modulation frequency, 0.15 mT
602 modulation amplitude, 0.6 - 2 mW microwave power, 5.12 ms time constant, 22.5 ms conversion time,
603 and 18 mT sweep width.

604

605 **Pulsed EPR measurements**

606 Pulsed EPR (PELDOR/DEER) experiments were performed on a Bruker Eleksys E580 Q-Band
607 (33.7 GHz) Pulsed ESR spectrometer equipped with an arbitrary waveform generator (SpinJet AWG,
608 Bruker), a 50 W solid state amplifier, a continuous-flow helium cryostat, and a temperature control
609 system (Oxford Instruments). Measurements were performed at 50 K using a 10 – 20 µL frozen sample
610 containing 15 – 20 % glycerol-*d*₈ in a 1.6 mm quartz ESR tubes (Suprasil, Wilmad LabGlass). For
611 measuring the phase memory times (T_M), a 48 ns $\pi/2$ - τ - π Gaussian pulse sequence was used with a
612 two-step phase cycling, while τ was increased in 4 ns steps. PELDOR measurements were performed
613 with a Bruker EN5107D2 dielectric resonator at 50 K using a dead-time free four-pulse sequence and a
614 16-step phase cycling cycling (x[x][x_p]x) [55,56]. A 38 ns Gaussian pulse (full width at half maximum
615 (FWHM) of 16.1 ns) was used as the pump pulse with a 48 ns (FWHM of 20.4 ns) Gaussian observer
616 pulses. The pump pulse was set to the maximum of the echo-detected field swept spectrum and the
617 observer pulses were set at 80 MHz lower. The deuterium modulations were averaged by increasing the
618 first interpulse delay by 16 ns for 8 steps. The five-pulse PELDOR/DEER experiments were performed
619 according to the pulse sequence $\pi/2_{\text{obs}} - (\tau/2 - t_0) - \pi_{\text{pump}} - t_0 - \pi_{\text{obs}} - t' - \pi_{\text{pump}} - (\tau - t' + \delta) - \pi_{\text{obs}} - (\tau_2$
620 $+ \delta)$. Experiments were performed at 50 K using 48 ns Gaussian observer pulses and a 16-step phase
621 cycling (xx_p [x] [x_p]x). A 36 ns pump pulse was used at $\nu_{\text{obs}} + 80$ MHz. Nuclear modulation averaging
622 was performed analogous to 4-pulse PELDOR (16 ns shift in 8 steps) with a corresponding shift of the
623 standing pump pulse. The four-pulse data analysis was performed using Tikhonov regularization as
624 implemented in the MATLAB-based DeerAnalysis2019 package [57]. The background arising from
625 intermolecular interactions were removed from the primary data $V(t)/V(0)$ and the resulting form factors

626 F(t)/F(0) were fitted with a model-free approach to distance distributions. For an error estimation of the
627 probability distribution, the distances for different background functions were determined through
628 gradually changing the time window and the dimensionality for the spin distribution (see Supplementary
629 Table S2). The data was additionally analyzed to predict the distances (and the background) in a user-
630 independent manner using the deep neural network (DEERNet) analysis, which is hosted by the
631 DeerAnalysis2019 package [58,59]. Samples for which both 4-pulse and 5-pulse data are available were
632 globally analyzed using the Python based DeerLab program [60]. Distance distributions for the
633 structures (PDB 8BJC and 1FD9) were simulated using a rotamer library approach using the MATLAB-
634 based MMM2022.2 software package [58].

635

636 **Small angle X-ray scattering (SAXS)**

637 SAXS experiments were carried out at the EMBL-P12 bioSAXS beam line, DESY [61]. SEC-SAXS
638 data were collected [62], $I(q)$ vs q , where $q = 4\pi\sin\theta/\lambda$ is the scattering angle and λ the X-ray wavelength
639 (0.124 nm; 10 keV). Data collection was carried out at 20 °C using a Superdex200 Increase 5/150
640 analytical SEC column (GE Healthcare) equilibrated in the appropriate buffers (see Table S3) at flow
641 rates of 0.3 mL/min. Automated sample injection and data collection were controlled using the
642 *BECQUEREL* beam line control software [63]. The SAXS intensities were measured from the
643 continuously-flowing column eluent as a continuous series of 0.25 s individual X-ray exposures, using
644 a Pilatus 6M 2D-area detector for a total of one column volume (ca. 600-3000 frames in total, see Table
645 S3). The radial averaging of the data one-dimensional $I(q)$ vs q profiles was carried out with the
646 SASFLOW pipeline incorporating RADAVER from the ATSAS 2.8 software suite [64]. The individual
647 frames obtained for each SEC-SAXS run were processed using CHROMIXS [65]. Briefly, individual
648 SAXS data frames were selected across the respective sample SEC-elution peaks and appropriate solute-
649 free buffer regions of the elution profile were identified, averaged and then subtracted to obtain
650 individual background-subtracted sample data frames. The radius of gyration (R_g) of each data frame
651 was assessed in CHROMIXS and frames with equivalent R_g were scaled and subsequently averaged to
652 produce the final one-dimensional and background-corrected SAXS profiles. Only those scaled
653 individual SAXS data frames with a consistent R_g through the SEC-elution peak that were also evaluated
654 as statistically similar through the measured q -range were included to produce the final SAXS profiles.
655 Corresponding UV traces were not measured; the column eluate was directly moved to the P12 sample
656 exposure unit after the SEC column, forgoing UV absorption measurements, to minimize unwanted
657 band-broadening of the sample. All SAXS data-data comparisons and data-model fits were assessed
658 using the reduced c^2 test and the Correlation Map, or CORMAP, p -value [66]. Fits within the c^2 range
659 of 0.9–1.1 or having CORMAP p -values higher than the significance threshold cutoff of $\alpha = 0.01$ are
660 considered excellent, i.e., absence of systematic differences between the data-data or data-model fits at
661 the significance threshold.

662 Primary SAXS data were analysed using PRIMUS as well as additional modules from the ATSAS 3.0.1
663 software suite [67]. R_g and the forward scattering at zero angle, $I(0)$ were estimated via the Guinier
664 approximation [68] ($\ln(I(q))$ vs. q^2 for $qR_g < 1.3$) and the real-space pair distance distribution function,
665 or $p(r)$ profile (calculated from the indirect inverse Fourier transformation of the data, thus also yielding
666 estimates of the maximum particle dimension, D_{max} , Porod volume, V_p , shape classification, and
667 concentration-independent molecular weight [69–71]). Dimensionless Kratky plot representations of the
668 SAXS data ($qR_g^2(I(q)/I(0))$ vs. qR_g) were generated as previously described [72]. All collected SAXS
669 data are reported in Tables S3.

670

671 **Rigid body modeling** – Rigid-body normal mode analysis of *LpMIP* was performed using the program
672 SREFLEX [73] using the *LpMIP apo* and JK095-bound X-ray crystal structures (PDB: 1FD9, 8BJD and
673 8BJC) as templates. CRY SOL was used to assess data-model fits [74].

674

675 **Thermal stability assay**

676 10 μ g of purified *LpMIP* constructs in 20 mM Tris pH 7, 150 mM NaCl were incubated with a final
677 concentration of 0.02 % DMSO or a 5-fold molar excess of JK095 in DMSO (0.02 % final
678 concentration). 2.5 μ L of a 50x SYPRO Orange (Merck) stock was added to each sample directly before
679 measurement of the melting temperature in a 96-well plate on a QuantStudio 1 Real-Time PCR System
680 reader (Thermo Fisher) with a temperature increase of 0.05 $^{\circ}$ C/min. The fluorescence of SYPRO Orange
681 was measured using the filter calibrated for SYBR GREEN with an excitation filter of 470 ± 15 nm and
682 an emission filter of 520 ± 15 nm.

683

684 **Data availability**

685 The coordinates of the refined models and structure factors have been deposited into the PDB repository:
686 8BJC for *LpMIP*¹⁻²¹³, 8BJD for *LpMIP*¹⁻²¹³JK095, 8BK6 for *LpMIP*¹⁰⁰⁻²¹³ JK095, 8BK5 for *LpMIP*⁷⁷⁻²¹³
687 JK095, 8BJE for *LpMIP*⁷⁷⁻²¹³ JK236 and 8BK4 for *TcMIP* JK236. The NMR backbone assignment of
688 *LpMIP*¹⁰⁰⁻²¹³ has been deposited in the BioMagResBank (www.bmrb.io) under the accession number
689 51861. The NMR backbone assignments for full-length *LpMIP*¹⁻²¹³ and *LpMIP*⁷⁷⁻²¹³ are available from
690 the BMRB under the accession numbers 7021 and 6334, respectively [38,75]. SAXS data for full-length
691 *LpMIP* have been deposited in the SASBDB under the accession numbers SASDSY6 (apo state),
692 SASDSZ6 (with JK095) and SASDS27 (with JK236).

693

694 **Conflict of interest**

695 The authors have no conflict of interest to declare.

696

697 **Author contributions**

698 Sample preparation: CW, VHPC, FT, BG; Biochemistry: VHCP, FT, BG; X-ray crystallography: JJW,
699 BG, AG; NMR spectroscopy: CW, VHPC, FT, BG; EPR spectroscopy: VHPC, MD, BJ; SAXS: CW,
700 FT, BG, JMH; Inhibitor synthesis: PK; Conceptualization: UAH; Funding acquisition: BJ, FH, AG,
701 UAH; Supervision: BG, BJ, FH, AG, UAH; Paper writing – first draft: UAH; Paper writing – review
702 and editing: CW, JJW, BG, BJ, AG, UAH; visualization: CW, JJW, VHPC, MD, BG, UAH. All authors
703 read and approved the final version of the manuscript.

704

705 **Acknowledgments**

706 We thank Sarah-Ana Mitrovic, Hannah Niederlechner, Sabine Häfner and Dania Rose-Sperling for
707 technical assistance and Robin Deutscher for support with synthesis. VHPC acknowledges a DAAD-
708 CONACYT PhD fellowship. BG acknowledges a PhD fellowship by the Max Planck Graduate Center
709 (MPGC). Access to beamline P12, DESY, Hamburg was made available via iNEXT-ERIC (BAG
710 proposal #SAXS-1106 (to UAH)). We are grateful to Shibom Basu and Montserrat Soler Lopez at the
711 ESRF for providing assistance at beamlines ID23-2 and ID30A-3 (BAG proposals #MX-2268 and #MX-
712 2407 to AG). We thank Andreas Schlundt for organizational support with SAXS measurements. We
713 thank the Centre of Biomolecular Magnetic Resonance (BMRZ) at the Goethe University Frankfurt
714 funded by the state of Hesse and the Jena School for Microbial Communication (JSMC) for support.
715 Funded by the Federal Ministry of Education and Research (BMBF) project iMIP (16GW0211 to FH,
716 16GW0214 to UAH). BJ acknowledges financial support through the Emmy Noether program (JO
717 1428/1-1) and a large equipment funding (438280639) from the Deutsche Forschungsgemeinschaft
718 (DFG). Supported by the DFG under Germany's Excellence Strategy - EXC 2051 - Project ID
719 390713860 and the collaborative research cluster SFB1127/3 ChemBioSys— Project ID 239748522 (to
720 UAH). UAH acknowledges an instrumentation grant by the REACT-EU EFRE Thuringia (Recovery
721 assistance for cohesion and the territories of Europe, European Fonds for Regional Development,
722 Thuringia) initiative of the European Union.

723 References

- 724 [1] J.E. Martyn, L. Gomez-Valero, C. Buchrieser, The evolution and role of eukaryotic-like domains
725 in environmental intracellular bacteria: the battle with a eukaryotic cell, *FEMS Microbiology*
726 *Reviews*. 46 (2022) fuac012. <https://doi.org/10.1093/femsre/fuac012>.
- 727 [2] I.G. Gonçalves, L.C. Simões, M. Simões, *Legionella pneumophila*, *Trends in Microbiology*. 29
728 (2021) 860–861. <https://doi.org/10.1016/j.tim.2021.04.005>.
- 729 [3] C.M. Anand, A.R. Skinner, A. Malic, J.B. Kurtz, Interaction of *L. pneumophila* and a free living
730 amoeba (*Acanthamoeba palestinensis*), *J Hyg (Lond)*. 91 (1983) 167–178.
- 731 [4] D. Chauhan, S.R. Shames, Pathogenicity and Virulence of *Legionella*: Intracellular replication
732 and host response, *Virulence*. 12 (n.d.) 1122–1144.
733 <https://doi.org/10.1080/21505594.2021.1903199>.
- 734 [5] M.F. Brady, V. Sundareshan, *Legionnaires' Disease*, in: *StatPearls*, StatPearls Publishing,
735 Treasure Island (FL), 2022. <http://www.ncbi.nlm.nih.gov/books/NBK430807/> (accessed
736 November 20, 2022).
- 737 [6] D. Viasus, V. Gaia, C. Manzur-Barbur, J. Carratalà, *Legionnaires' Disease: Update on Diagnosis*
738 *and Treatment*, *Infect Dis Ther*. 11 (2022) 973–986. [https://doi.org/10.1007/s40121-022-
739 *00635-7*.](https://doi.org/10.1007/s40121-022-00635-7)
- 740 [7] J. Hacker, M. Ott, E. Wintermeyer, B. Ludwig, G. Fischer, Analysis of virulence factors of
741 *Legionella pneumophila*, *Zentralbl Bakteriologie*. 278 (1993) 348–358.
742 [https://doi.org/10.1016/s0934-8840\(11\)80851-0](https://doi.org/10.1016/s0934-8840(11)80851-0).
- 743 [8] N.C. Engleberg, C. Carter, D.R. Weber, N.P. Cianciotto, B.I. Eisenstein, DNA sequence of mip, a
744 *Legionella pneumophila* gene associated with macrophage infectivity, *Infect Immun*. 57 (1989)
745 1263–1270. <https://doi.org/10.1128/iai.57.4.1263-1270.1989>.
- 746 [9] N.P. Cianciotto, B.I. Eisenstein, C.H. Mody, G.B. Toews, N.C. Engleberg, A *Legionella*
747 *pneumophila* gene encoding a species-specific surface protein potentiates initiation of
748 intracellular infection, *Infect Immun*. 57 (1989) 1255–1262.
749 <https://doi.org/10.1128/iai.57.4.1255-1262.1989>.
- 750 [10] N.P. Cianciotto, B.I. Eisenstein, C.H. Mody, N.C. Engleberg, A mutation in the mip gene results in
751 an attenuation of *Legionella pneumophila* virulence, *J Infect Dis*. 162 (1990) 121–126.
752 <https://doi.org/10.1093/infdis/162.1.121>.
- 753 [11] J. Rasch, C.M. Ünal, A. Klages, Ü. Karsli, N. Heinsohn, R.M.H.J. Brouwer, M. Richter, A.
754 Dellmann, M. Steinert, Peptidyl-Prolyl-cis/trans-Isomerases Mip and PpiB of *Legionella*
755 *pneumophila* Contribute to Surface Translocation, Growth at Suboptimal Temperature, and
756 Infection, *Infect Immun*. 87 (2018) e00939-17. <https://doi.org/10.1128/IAI.00939-17>.
- 757 [12] N.P. Cianciotto, B.S. Fields, *Legionella pneumophila* mip gene potentiates intracellular infection
758 of protozoa and human macrophages, *Proc Natl Acad Sci U S A*. 89 (1992) 5188–5191.
759 <https://doi.org/10.1073/pnas.89.11.5188>.
- 760 [13] B. Schmidt, J. Rahfeld, A. Schierhorn, B. Ludwig, J. Hacker, G. Fischer, A homodimer represents
761 an active species of the peptidyl-prolyl cis/trans isomerase FKBP25mem from *Legionella*
762 *pneumophila*, *FEBS Lett*. 352 (1994) 185–190. [https://doi.org/10.1016/0014-5793\(94\)00970-8](https://doi.org/10.1016/0014-5793(94)00970-8).
- 763 [14] A. Riboldi-Tunnicliffe, B. König, S. Jessen, M.S. Weiss, J. Rahfeld, J. Hacker, G. Fischer, R.
764 Hilgenfeld, Crystal structure of Mip, a prolyl isomerase from *Legionella pneumophila*, *Nat Struct*
765 *Mol Biol*. 8 (2001) 779–783. <https://doi.org/10.1038/nsb0901-779>.
- 766 [15] G. Fischer, H. Bang, B. Ludwig, K. Mann, J. Hacker, Mip protein of *Legionella pneumophila*
767 exhibits peptidyl-prolyl-cis/trans isomerase (PPIase) activity, *Molecular Microbiology*. 6 (1992)
768 1375–1383. <https://doi.org/10.1111/j.1365-2958.1992.tb00858.x>.
- 769 [16] M.W. Harding, A. Galat, D.E. Uehling, S.L. Schreiber, A receptor for the immuno-suppressant
770 FK506 is a cis–trans peptidyl-prolyl isomerase, *Nature*. 341 (1989) 758–760.
771 <https://doi.org/10.1038/341758a0>.
- 772 [17] J.J. Siekierka, S.H.Y. Hung, M. Poe, C.S. Lin, N.H. Sigal, A cytosolic binding protein for the
773 immunosuppressant FK506 has peptidyl-prolyl isomerase activity but is distinct from
774 cyclophilin, *Nature*. 341 (1989) 755–757. <https://doi.org/10.1038/341755a0>.

- 775 [18] C.B. Kang, Y. Hong, S. Dhe-Paganon, H.S. Yoon, FKBP family proteins: immunophilins with
776 versatile biological functions, *Neurosignals*. 16 (2008) 318–325.
777 <https://doi.org/10.1159/000123041>.
- 778 [19] C. Ünal, K.F. Schwedhelm, A. Thiele, M. Weiwad, K. Schweimer, F. Frese, G. Fischer, J. Hacker, C.
779 Faber, M. Steinert, Collagen IV-derived peptide binds hydrophobic cavity of Legionella
780 pneumophila Mip and interferes with bacterial epithelial transmigration, *Cellular Microbiology*.
781 13 (2011) 1558–1572. <https://doi.org/10.1111/j.1462-5822.2011.01641.x>.
- 782 [20] C. Wagner, A.S. Khan, T. Kamphausen, B. Schmausser, C. Ünal, U. Lorenz, G. Fischer, J. Hacker,
783 M. Steinert, Collagen binding protein Mip enables Legionella pneumophila to transmigrate
784 through a barrier of NCI-H292 lung epithelial cells and extracellular matrix, *Cellular*
785 *Microbiology*. 9 (2007) 450–462. <https://doi.org/10.1111/j.1462-5822.2006.00802.x>.
- 786 [21] A. Ceymann, M. Horstmann, P. Ehses, K. Schweimer, A.-K. Paschke, M. Steinert, C. Faber,
787 Solution structure of the Legionella pneumophila Mip-rapamycin complex, *BMC Struct Biol*. 8
788 (2008) 17. <https://doi.org/10.1186/1472-6807-8-17>.
- 789 [22] A.G. Lundemose, S. Birkelund, S.J. Fey, P.M. Larsen, G. Christiansen, Chlamydia trachomatis
790 contains a protein similar to the Legionella pneumophila mip gene product, *Mol Microbiol*. 5
791 (1991) 109–115. <https://doi.org/10.1111/j.1365-2958.1991.tb01831.x>.
- 792 [23] R. Leuzzi, L. Serino, M. Scarselli, S. Savino, M.R. Fontana, E. Monaci, A. Taddei, G. Fischer, R.
793 Rappuoli, M. Pizza, Ng-MIP, a surface-exposed lipoprotein of Neisseria gonorrhoeae, has a
794 peptidyl-prolyl cis/trans isomerase (PPIase) activity and is involved in persistence in
795 macrophages, *Mol Microbiol*. 58 (2005) 669–681. <https://doi.org/10.1111/j.1365-2958.2005.04859.x>.
- 796 [24] S.M. Horne, T.J. Kottom, L.K. Nolan, K.D. Young, Decreased intracellular survival of an fkpA
797 mutant of Salmonella typhimurium Copenhagen, *Infect Immun*. 65 (1997) 806–810.
798 <https://doi.org/10.1128/iai.65.2.806-810.1997>.
- 800 [25] Q. Huang, J. Yang, C. Li, Y. Song, Y. Zhu, N. Zhao, X. Mou, X. Tang, G. Luo, A. Tong, B. Sun, H.
801 Tang, H. Li, L. Bai, R. Bao, Structural characterization of PaFkbA: A periplasmic chaperone from
802 Pseudomonas aeruginosa, *Computational and Structural Biotechnology Journal*. 19 (2021)
803 2460–2467. <https://doi.org/10.1016/j.csbj.2021.04.045>.
- 804 [26] P.J.B. Pereira, M.C. Vega, E. González-Rey, R. Fernández-Carazo, S. Macedo-Ribeiro, F.X. Gomis-
805 Rüth, A. González, M. Coll, Trypanosoma cruzi macrophage infectivity potentiator has a
806 rotamase core and a highly exposed α -helix, *EMBO Reports*. 3 (2002) 88–94.
807 <https://doi.org/10.1093/embo-reports/kvf009>.
- 808 [27] A. Moro, F. Ruiz-Cabello, A. Fernández-Cano, R.P. Stock, A. González, Secretion by Trypanosoma
809 cruzi of a peptidyl-prolyl cis-trans isomerase involved in cell infection., *EMBO J*. 14 (1995) 2483–
810 2490.
- 811 [28] L.M.D. Magalhães, K.J. Gollob, B. Zingales, W.O. Dutra, Pathogen diversity, immunity, and the
812 fate of infections: lessons learned from Trypanosoma cruzi human-host interactions, *Lancet*
813 *Microbe*. 3 (2022) e711–e722. [https://doi.org/10.1016/S2666-5247\(21\)00265-2](https://doi.org/10.1016/S2666-5247(21)00265-2).
- 814 [29] C.M. Ünal, M. Steinert, Microbial peptidyl-prolyl cis/trans isomerases (PPIases): virulence
815 factors and potential alternative drug targets, *Microbiol Mol Biol Rev*. 78 (2014) 544–571.
816 <https://doi.org/10.1128/MMBR.00015-14>.
- 817 [30] J.M. Kolos, A.M. Voll, M. Bauder, F. Hausch, FKBP Ligands-Where We Are and Where to Go?,
818 *Front Pharmacol*. 9 (2018) 1425. <https://doi.org/10.3389/fphar.2018.01425>.
- 819 [31] N.J. Scheuplein, N.M. Bzdyl, E.A. Kibble, T. Lohr, U. Holzgrabe, M. Sarkar-Tyson, Targeting
820 Protein Folding: A Novel Approach for the Treatment of Pathogenic Bacteria, *J Med Chem*. 63
821 (2020) 13355–13388. <https://doi.org/10.1021/acs.jmedchem.0c00911>.
- 822 [32] I.H. Norville, N.J. Harmer, S.V. Harding, G. Fischer, K.E. Keith, K.A. Brown, M. Sarkar-Tyson, R.W.
823 Titball, A Burkholderia pseudomallei Macrophage Infectivity Potentiator-Like Protein Has
824 Rapamycin-Inhibitable Peptidylprolyl Isomerase Activity and Pleiotropic Effects on Virulence ∇ ,
825 *Infect Immun*. 79 (2011) 4299–4307. <https://doi.org/10.1128/IAI.00134-11>.

- 826 [33] I.H. Norville, K. O’Shea, M. Sarkar-Tyson, S. Zheng, R.W. Titball, G. Varani, N.J. Harmer, The
827 structure of a *Burkholderia pseudomallei* immunophilin–inhibitor complex reveals new
828 approaches to antimicrobial development, *Biochemical Journal*. 437 (2011) 413–422.
829 <https://doi.org/10.1042/BJ20110345>.
- 830 [34] S. Pomplun, C. Sippel, A. Hähle, D. Tay, K. Shima, A. Klages, C.M. Ünal, B. Rieß, H.T. Toh, G.
831 Hansen, H.S. Yoon, A. Bracher, P. Preiser, J. Rupp, M. Steinert, F. Hausch, Chemogenomic
832 Profiling of Human and Microbial FK506-Binding Proteins, *J Med Chem*. 61 (2018) 3660–3673.
833 <https://doi.org/10.1021/acs.jmedchem.8b00137>.
- 834 [35] C.M. Ünal, M. Steinert, FKBP in bacterial infections, *Biochim Biophys Acta*. 1850 (2015) 2096–
835 2102. <https://doi.org/10.1016/j.bbagen.2014.12.018>.
- 836 [36] S. Khan, S. Khan, S. Baboota, J. Ali, Immunosuppressive drug therapy – biopharmaceutical
837 challenges and remedies, *Expert Opinion on Drug Delivery*. 12 (2015) 1333–1349.
838 <https://doi.org/10.1517/17425247.2015.1005072>.
- 839 [37] M.V. Petoukhov, D.I. Svergun, Global Rigid Body Modeling of Macromolecular Complexes
840 against Small-Angle Scattering Data, *Biophysical Journal*. 89 (2005) 1237–1250.
841 <https://doi.org/10.1529/biophysj.105.064154>.
- 842 [38] M. Horstmann, T. Kamphausen, K. Schweimer, M. Steinert, J. Hacker, A. Haase, P. Rösch, G.
843 Schweimer, C. Faber, Letter to the Editor: 1H, 13C, 15N backbone and sidechain resonance
844 assignment of Mip(77–213) the PPIase domain of the Legionella pneumophila Mip protein, *J*
845 *Biomol NMR*. 31 (2005) 77–78. <https://doi.org/10.1007/s10858-004-6041-6>.
- 846 [39] R. Deutscher, S. Karagöz, P. Purder, J. Kolos, C. Meyners, W. Sugiarto, P. Krajczyk, F. Tebbe, T.
847 Geiger, C. Ünal, U. Hellmich, M. Steinert, F. Hausch, [4.3.1] Bicyclic FKBP ligands inhibit
848 Legionella pneumophila infection by *LpMip*-dependent and *LpMip* independent mechanisms,
849 (2023). <https://doi.org/10.26434/chemrxiv-2023-vfssm>.
- 850 [40] P. Rossi, G.V.T. Swapna, Y.J. Huang, J.M. Aramini, C. Anklin, K. Conover, K. Hamilton, R. Xiao,
851 T.B. Acton, A. Ertekin, J.K. Everett, G.T. Montelione, A microscale protein NMR sample
852 screening pipeline, *J Biomol NMR*. 46 (2010) 11–22. [https://doi.org/10.1007/s10858-009-9386-
853 z](https://doi.org/10.1007/s10858-009-9386-
853 z).
- 854 [41] J.M. Kolos, S. Pomplun, S. Jung, B. Rieß, P.L. Purder, A.M. Voll, S. Merz, M. Gnatzy, T.M. Geiger,
855 I. Quist-Løkken, J. Jatzlau, P. Knaus, T. Holien, A. Bracher, C. Meyners, P. Czodrowski, V.
856 Krewald, F. Hausch, Picomolar FKBP inhibitors enabled by a single water-displacing methyl
857 group in bicyclic [4.3.1] aza-amides, *Chem. Sci*. 12 (2021) 14758–14765.
858 <https://doi.org/10.1039/D1SC04638A>.
- 859 [42] K. Hu, V. Galius, K. Pervushin, Structural Plasticity of Peptidyl–Prolyl Isomerase sFkpA Is a Key to
860 Its Chaperone Function As Revealed by Solution NMR, *Biochemistry*. 45 (2006) 11983–11991.
861 <https://doi.org/10.1021/bi0607913>.
- 862 [43] R.B. Best, K. Lindorff-Larsen, M.A. DePristo, M. Vendruscolo, Relation between native
863 ensembles and experimental structures of proteins, *Proceedings of the National Academy of*
864 *Sciences*. 103 (2006) 10901–10906. <https://doi.org/10.1073/pnas.0511156103>.
- 865 [44] P.K.A. Jagtap, S. Asami, C. Sippel, V.R.I. Kaila, F. Hausch, M. Sattler, Selective Inhibitors of
866 FKBP51 Employ Conformational Selection of Dynamic Invisible States, *Angewandte Chemie*
867 *International Edition*. 58 (2019) 9429–9433. <https://doi.org/10.1002/anie.201902994>.
- 868 [45] W. Kabsch, Integration, scaling, space-group assignment and post-refinement, *Acta Cryst D*. 66
869 (2010) 133–144. <https://doi.org/10.1107/S0907444909047374>.
- 870 [46] A.J. McCoy, R.W. Grosse-Kunstleve, P.D. Adams, M.D. Winn, L.C. Storoni, R.J. Read, Phaser
871 crystallographic software, *J Appl Cryst*. 40 (2007) 658–674.
872 <https://doi.org/10.1107/S0021889807021206>.
- 873 [47] P. Emsley, B. Lohkamp, W.G. Scott, K. Cowtan, Features and development of Coot, *Acta Cryst D*.
874 66 (2010) 486–501. <https://doi.org/10.1107/S0907444910007493>.
- 875 [48] G.N. Murshudov, A.A. Vagin, E.J. Dodson, Refinement of Macromolecular Structures by the
876 Maximum-Likelihood Method, *Acta Cryst D*. 53 (1997) 240–255.
877 <https://doi.org/10.1107/S0907444996012255>.

- 878 [49] E.F. Pettersen, T.D. Goddard, C.C. Huang, E.C. Meng, G.S. Couch, T.I. Croll, J.H. Morris, T.E.
879 Ferrin, UCSF ChimeraX: Structure visualization for researchers, educators, and developers,
880 Protein Science. 30 (2021) 70–82. <https://doi.org/10.1002/pro.3943>.
- 881 [50] D.S. Wishart, C.G. Bigam, J. Yao, F. Abildgaard, H.J. Dyson, E. Oldfield, J.L. Markley, B.D. Sykes,
882 ¹H, ¹³C and ¹⁵N chemical shift referencing in biomolecular NMR, J Biomol NMR. 6 (1995) 135–
883 140. <https://doi.org/10.1007/BF00211777>.
- 884 [51] W.F. Vranken, W. Boucher, T.J. Stevens, R.H. Fogh, A. Pajon, M. Llinas, E.L. Ulrich, J.L. Markley,
885 J. Ionides, E.D. Laue, The CCPN data model for NMR spectroscopy: Development of a software
886 pipeline, Proteins: Structure, Function, and Bioinformatics. 59 (2005) 687–696.
887 <https://doi.org/10.1002/prot.20449>.
- 888 [52] M.W. Maciejewski, A.D. Schuyler, M.R. Gryk, I.I. Moraru, P.R. Romero, E.L. Ulrich, H.R.
889 Eghbalnia, M. Livny, F. Delaglio, J.C. Hoch, NMRbox: A Resource for Biomolecular NMR
890 Computation, Biophysical Journal. 112 (2017) 1529–1534.
891 <https://doi.org/10.1016/j.bpj.2017.03.011>.
- 892 [53] M.P. Williamson, Using chemical shift perturbation to characterise ligand binding, Prog Nucl
893 Magn Reson Spectrosc. 73 (2013) 1–16. <https://doi.org/10.1016/j.pnmrs.2013.02.001>.
- 894 [54] L.E. Kay, D.A. Torchia, A. Bax, Backbone dynamics of proteins as studied by nitrogen-15 inverse
895 detected heteronuclear NMR spectroscopy: application to staphylococcal nuclease,
896 Biochemistry. 28 (1989) 8972–8979. <https://doi.org/10.1021/bi00449a003>.
- 897 [55] M. Pannier, S. Veit, A. Godt, G. Jeschke, H.W. Spiess, Dead-Time Free Measurement of Dipole–
898 Dipole Interactions between Electron Spins, Journal of Magnetic Resonance. 142 (2000) 331–
899 340. <https://doi.org/10.1006/jmre.1999.1944>.
- 900 [56] C.E. Tait, S. Stoll, Coherent pump pulses in Double Electron Electron Resonance spectroscopy,
901 Phys. Chem. Chem. Phys. 18 (2016) 18470–18485. <https://doi.org/10.1039/C6CP03555H>.
- 902 [57] G. Jeschke, V. Chechik, P. Ionita, A. Godt, H. Zimmermann, J. Banham, C.R. Timmel, D. Hilger, H.
903 Jung, DeerAnalysis2006—a comprehensive software package for analyzing pulsed ELDOR data,
904 Appl. Magn. Reson. 30 (2006) 473–498. <https://doi.org/10.1007/BF03166213>.
- 905 [58] Y. Polyhach, E. Bordignon, G. Jeschke, Rotamer libraries of spin labelled cysteines for protein
906 studies, Phys. Chem. Chem. Phys. 13 (2011) 2356–2366. <https://doi.org/10.1039/C0CP01865A>.
- 907 [59] S.G. Worswick, J.A. Spencer, G. Jeschke, I. Kuprov, Deep neural network processing of DEER
908 data, Science Advances. 4 (2018) eaat5218. <https://doi.org/10.1126/sciadv.aat5218>.
- 909 [60] L. Fábregas Ibáñez, G. Jeschke, S. Stoll, DeerLab: a comprehensive software package for
910 analyzing dipolar electron paramagnetic resonance spectroscopy data, Magnetic Resonance. 1
911 (2020) 209–224. <https://doi.org/10.5194/mr-1-209-2020>.
- 912 [61] C.E. Blanchet, A. Spilotros, F. Schwemmer, M.A. Graewert, A. Kikhney, C.M. Jeffries, D. Franke,
913 D. Mark, R. Zengerle, F. Cipriani, S. Fiedler, M. Roessle, D.I. Svergun, Versatile sample
914 environments and automation for biological solution X-ray scattering experiments at the P12
915 beamline (PETRA III, DESY), J Appl Cryst. 48 (2015) 431–443.
916 <https://doi.org/10.1107/S160057671500254X>.
- 917 [62] M.A. Graewert, S. Da Vela, T.W. Gräwert, D.S. Molodenskiy, C.E. Blanchet, D.I. Svergun, C.M.
918 Jeffries, Adding Size Exclusion Chromatography (SEC) and Light Scattering (LS) Devices to Obtain
919 High-Quality Small Angle X-Ray Scattering (SAXS) Data, Crystals. 10 (2020) 975.
920 <https://doi.org/10.3390/cryst10110975>.
- 921 [63] N.R. Hajizadeh, D. Franke, D.I. Svergun, Integrated beamline control and data acquisition for
922 small-angle X-ray scattering at the P12 BioSAXS beamline at PETRAIII storage ring DESY, J
923 Synchrotron Rad. 25 (2018) 906–914. <https://doi.org/10.1107/S1600577518005398>.
- 924 [64] D. Franke, A.G. Kikhney, D.I. Svergun, Automated acquisition and analysis of small angle X-ray
925 scattering data, Nuclear Instruments and Methods in Physics Research Section A: Accelerators,
926 Spectrometers, Detectors and Associated Equipment. 689 (2012) 52–59.
927 <https://doi.org/10.1016/j.nima.2012.06.008>.

- 928 [65] A. Panjkovich, D.I. Svergun, CHROMIXS: automatic and interactive analysis of chromatography-
929 coupled small-angle X-ray scattering data, *Bioinformatics*. 34 (2018) 1944–1946.
930 <https://doi.org/10.1093/bioinformatics/btx846>.
- 931 [66] D. Franke, C.M. Jeffries, D.I. Svergun, Correlation Map, a goodness-of-fit test for one-
932 dimensional X-ray scattering spectra, *Nat Methods*. 12 (2015) 419–422.
933 <https://doi.org/10.1038/nmeth.3358>.
- 934 [67] K. Manalastas-Cantos, P.V. Konarev, N.R. Hajizadeh, A.G. Kikhney, M.V. Petoukhov, D.S.
935 Molodenskiy, A. Panjkovich, H.D.T. Mertens, A. Gruzinov, C. Borges, C.M. Jeffries, D.I. Svergun,
936 D. Franke, ATSAS 3.0: expanded functionality and new tools for small-angle scattering data
937 analysis, *J Appl Cryst*. 54 (2021) 343–355. <https://doi.org/10.1107/S1600576720013412>.
- 938 [68] A. Guinier, La diffraction des rayons X aux très petits angles : application à l'étude de
939 phénomènes ultramicroscopiques, *Ann. Phys.* 11 (1939) 161–237.
940 <https://doi.org/10.1051/anphys/193911120161>.
- 941 [69] D.I. Svergun, Determination of the regularization parameter in indirect-transform methods
942 using perceptual criteria, *J Appl Cryst*. 25 (1992) 495–503.
943 <https://doi.org/10.1107/S0021889892001663>.
- 944 [70] N.R. Hajizadeh, D. Franke, C.M. Jeffries, D.I. Svergun, Consensus Bayesian assessment of protein
945 molecular mass from solution X-ray scattering data, *Sci Rep*. 8 (2018) 7204.
946 <https://doi.org/10.1038/s41598-018-25355-2>.
- 947 [71] D. Franke, C.M. Jeffries, D.I. Svergun, Machine Learning Methods for X-Ray Scattering Data
948 Analysis from Biomacromolecular Solutions, *Biophysical Journal*. 114 (2018) 2485–2492.
949 <https://doi.org/10.1016/j.bpj.2018.04.018>.
- 950 [72] V. Receveur-Brechot, D. Durand, How random are intrinsically disordered proteins? A small
951 angle scattering perspective, *Curr Protein Pept Sci*. 13 (2012) 55–75.
952 <https://doi.org/10.2174/138920312799277901>.
- 953 [73] A. Panjkovich, D.I. Svergun, Deciphering conformational transitions of proteins by small angle X-
954 ray scattering and normal mode analysis, *Phys. Chem. Chem. Phys.* 18 (2016) 5707–5719.
955 <https://doi.org/10.1039/C5CP04540A>.
- 956 [74] D. Svergun, C. Barberato, M.H.J. Koch, CRY SOL – a Program to Evaluate X-ray Solution
957 Scattering of Biological Macromolecules from Atomic Coordinates, *J Appl Cryst*. 28 (1995) 768–
958 773. <https://doi.org/10.1107/S0021889895007047>.
- 959 [75] M. Horstmann, P. Ehses, K. Schweimer, M. Steinert, T. Kamphausen, G. Fischer, J. Hacker, P.
960 Rösch, C. Faber, Domain Motions of the Mip Protein from *Legionella pneumophila*,
961 *Biochemistry*. 45 (2006) 12303–12311. <https://doi.org/10.1021/bi060818i>.
962

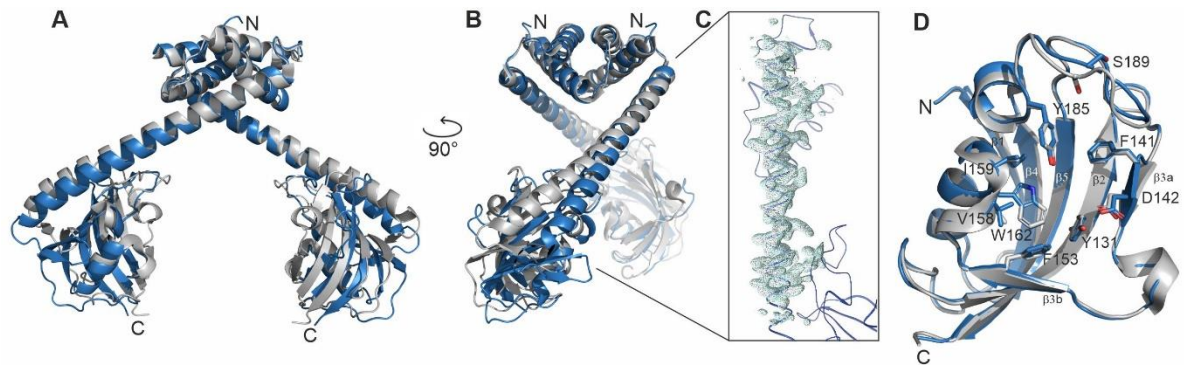
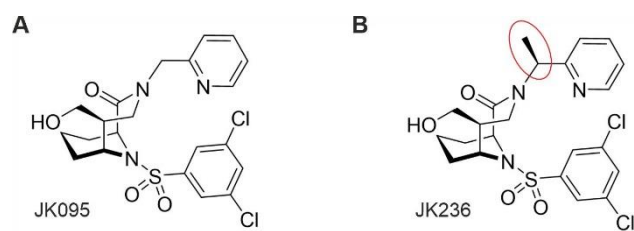


Fig. 1: Comparison of full-length *LpMIP* structures reveal stalk helix splaying.

(A, B) Overlay of the N-terminal dimerization domains of the two currently available *LpMIP*¹⁻²¹³ structures (PDB: 1FD9 at 2.41 Å, grey; PDB: 8BJC at 1.71 Å, blue) shows ~18° stalk helix splaying.

(C) Importantly, the stalk helix backbone of our newly determined *LpMIP* structure (blue) can be unambiguously placed in the 2Fo–Fc electron density map, shown here as a light blue mesh at 3σ. For clarity, only the density map for the stalk helix backbone is shown.

(D) Overlay of the FKBP-like domains from the two *LpMIP* structures. Residues surrounding the active site are shown as sticks, β-strands are labeled.



Scheme 1: [4.3.1]-aza-bicyclic sulfonamide inhibitors used in this study. JK095 (A) and JK236 (B) differ by the insertion of a stereospecific methyl group in the pyridine linker.

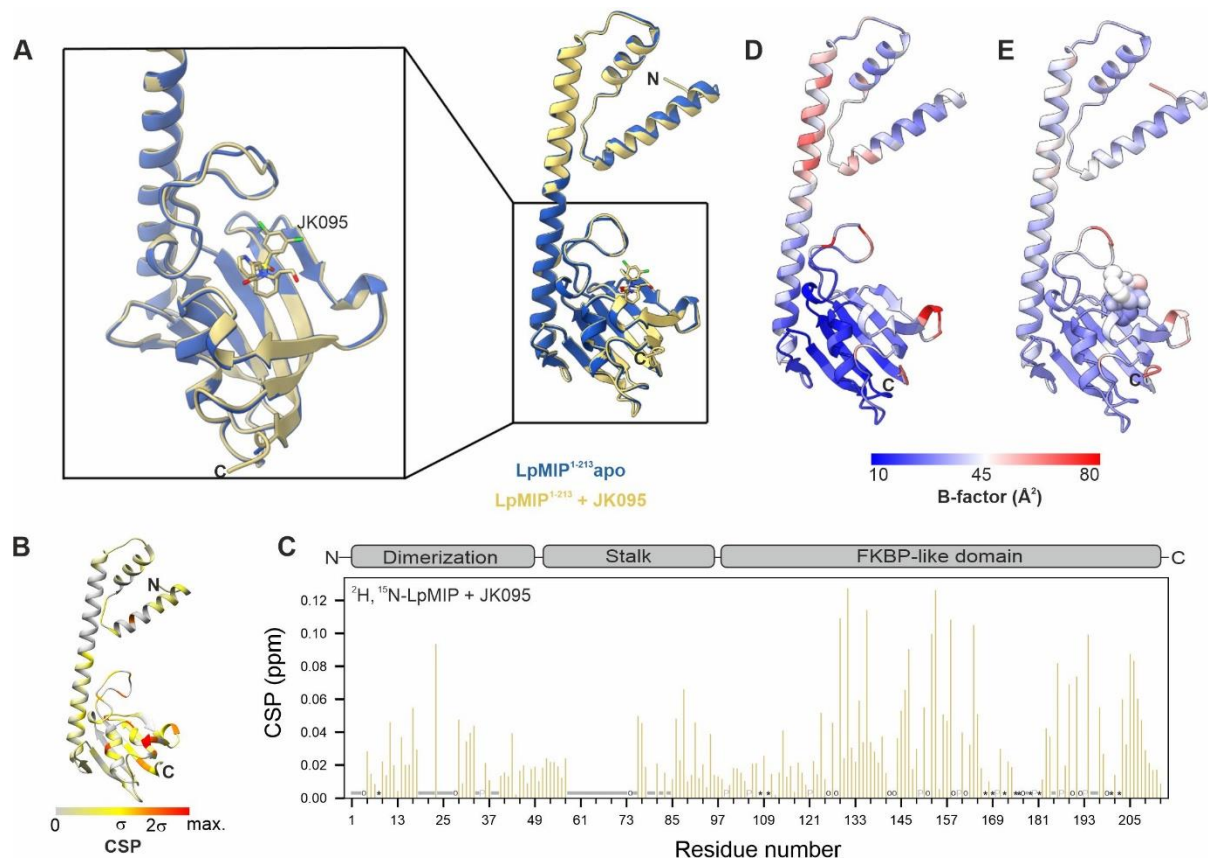


Fig. 2: Comparison of full-length *LpMIP* in the absence and presence of a bicyclic inhibitor.

(A) Overlay of *LpMIP* in the absence (blue, PDB: 8BJC) and presence of JK095 (yellow, PDB: 8BJD). The two structures align with a backbone RMSD of 0.349 \AA . In the zoom of the FKBP-like domain, JK095 is shown as sticks. Non-carbon atom color scheme: blue: N, red: O, yellow: S, green: Cl. Note that the orientation of the zoom has been slightly tilted to better visualize the structural differences in the $\beta 4/\beta 5$ -loop.

(B, C) Chemical shift changes in ^2H , ^{15}N -labeled *LpMIP* titrated with JK095 mapped on the *LpMIP* crystal structure (B) and per residue (C) with the protein topology shown on top for orientation. Proline residues and residues without assignment in either state are labeled with grey P or indicated by a grey bar, respectively. Black circles (apo) and asterisk (JK095) represent resonances present only in one state.

(D, E) Crystallographic B-factors of *LpMIP* in the absence (D) and presence (E) of JK095.

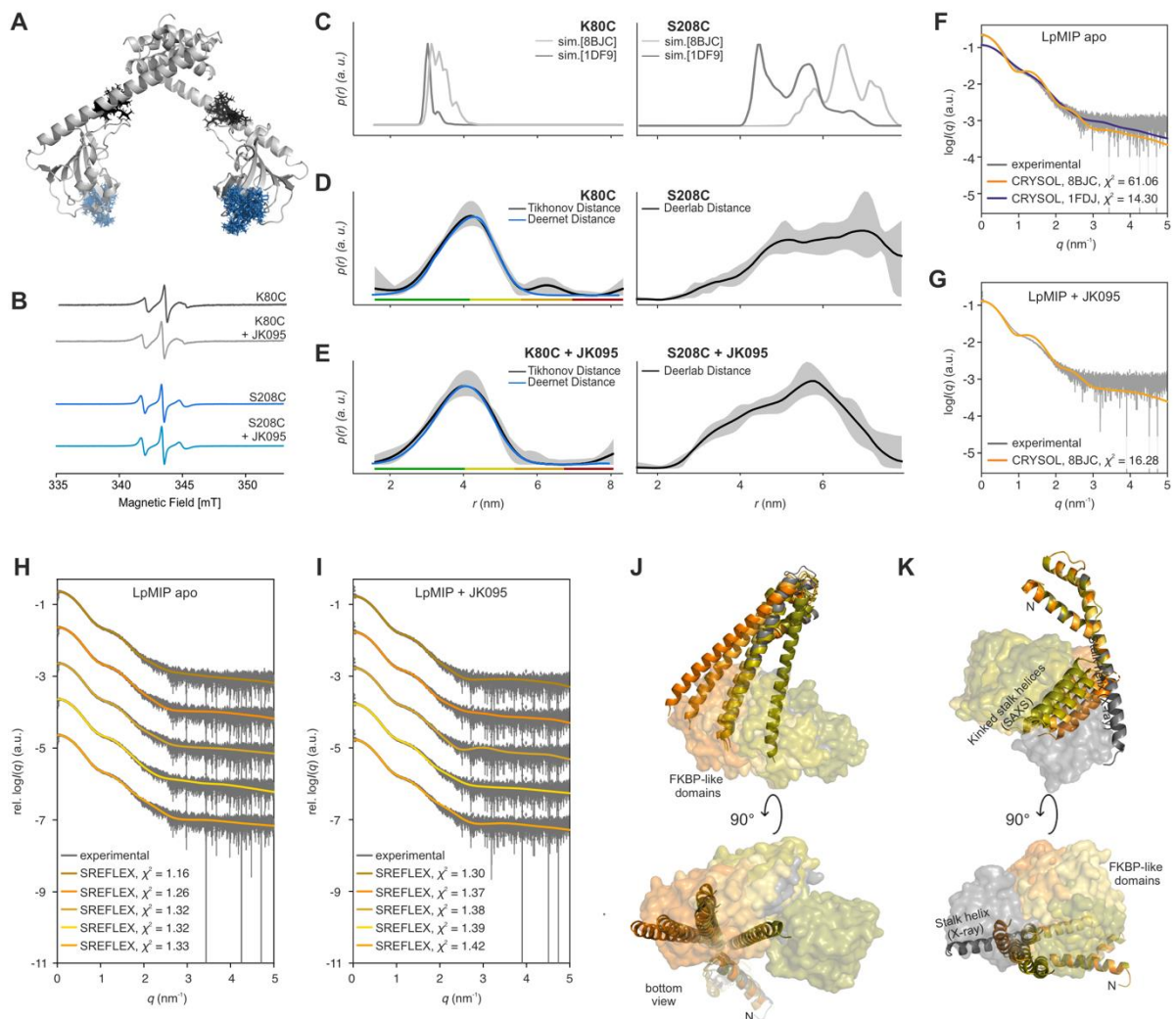


Fig. 3: Structural dynamics of full-length *LpMIP* in solution.

(A) Simulated rotamers of proxyl-spin labels attached to *LpMIP* at position K80C (black) or S208C (teal) (on PDB: 8BJC using MATLAB-based MMM2022.2 software).

(B) Continuous-wave EPR spectra of spin-labeled *LpMIP* single-cysteine variants.

(C) Predicted interspin distances (sim.) for *LpMIP* K80C (left) and *LpMIP* S208C (right) based on the available *apo* state crystal structures (PDB-IDs: 8BJC, 1FD9). (D, E) Measured spin label distances using PELDOR/DEER spectroscopy in the absence (D) and presence (E) of JK095. For *LpMIP* S208C, distances were determined through a global analysis of 4-pulse and 5-pulse PELDOR data (see Fig. S5). The rainbow code at the bottom indicates reliability for the probability distribution. (Green: shape, width and mean reliable; yellow: width and mean reliable, orange: mean reliable; red: not reliable)

(F, G) SAXS scattering data for *LpMIP* in the absence (F) and presence of JK095 (G). The simulated scattering curves (orange and blue traces) based on the available X-ray structures of *apo LpMIP* (PDB: 8BJC, 1F9J) and with JK095 (PDB: 8BJD) do not match the scattering profile of the protein in solution after least-square fit to experimental values for $0.5 \text{ nm}^{-1} < q < 1.5 \text{ nm}^{-1}$.

(H, I, J, K) For a better fit with the experimental SAXS data of *LpMIP* in solution in the *apo* (H) and the JK095 bound state (I), SREFLEX modeling was carried out and yielded the calculated scattering profiles shown in the log plots and *LpMIP* structural models with straight (J) and kinked (K) stalk helices. Accordingly, also the relative

orientation of the FKBP like domains (shown as transparent surfaces) changes dramatically. The X-ray structure (PBD: 8BJC) is shown in grey, representative SREFLEX models in orange hues. For better visualization, models with straight and kinked helices are shown in separate chains. There are no discernible differences between the *apo* and JK095-bound state in the *LpMIP* SREFLEX models, thus only the *apo* models are shown (for details see main text).

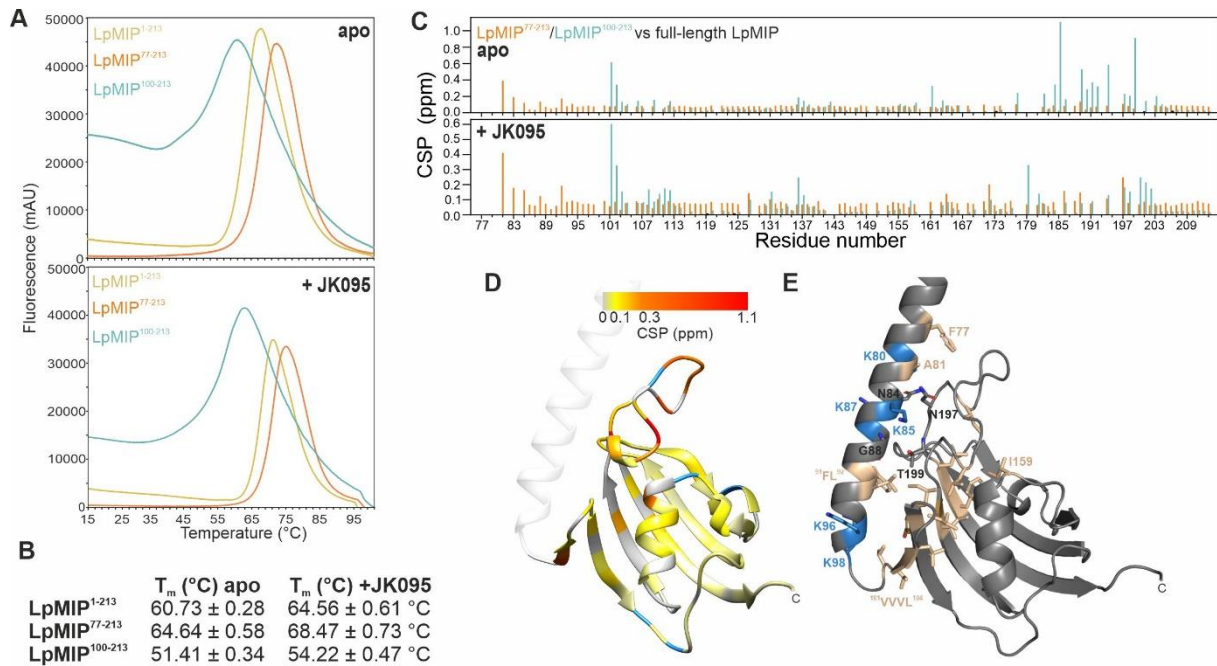


Fig. 4: Role of the *LpMIP* appendage domains for protein stability and crosstalk with the FKBP-like domain.

(A) Fluorescence-based melting assay. The melting temperature (T_m) for full-length *LpMIP* (yellow) or two deletion constructs (orange, cyan) in the absence (top) or presence of a three-fold molar excess of JK095 (bottom) can be obtained from the inversion point of the upward slope.

(B) T_m values for the three constructs obtained from the curves shown in (A). Errors are standard deviations from three replicates.

(C) Chemical shift perturbations of the FKBP-like domain resonances of *LpMIP*⁷⁷⁻²¹³ and *LpMIP*¹⁰⁰⁻²¹³ compared to full-length *LpMIP* (orange and blue, respectively) in the *apo* state (top) and with JK095 (bottom). (D) Chemical shift differences between full-length *LpMIP* and *LpMIP*¹⁰⁰⁻²¹³ mapped on the FKBP-like domain, residues for which no signal is observed in *LpMIP*¹⁰⁰⁻²¹³ are colored blue.

(E) Details of hydrophobic interaction network between stalk helix and FKBP-like domain. Hydrophobic residues shown in sand, basic residues in blue, all others in grey. For a better overview, not all sidechains are shown.

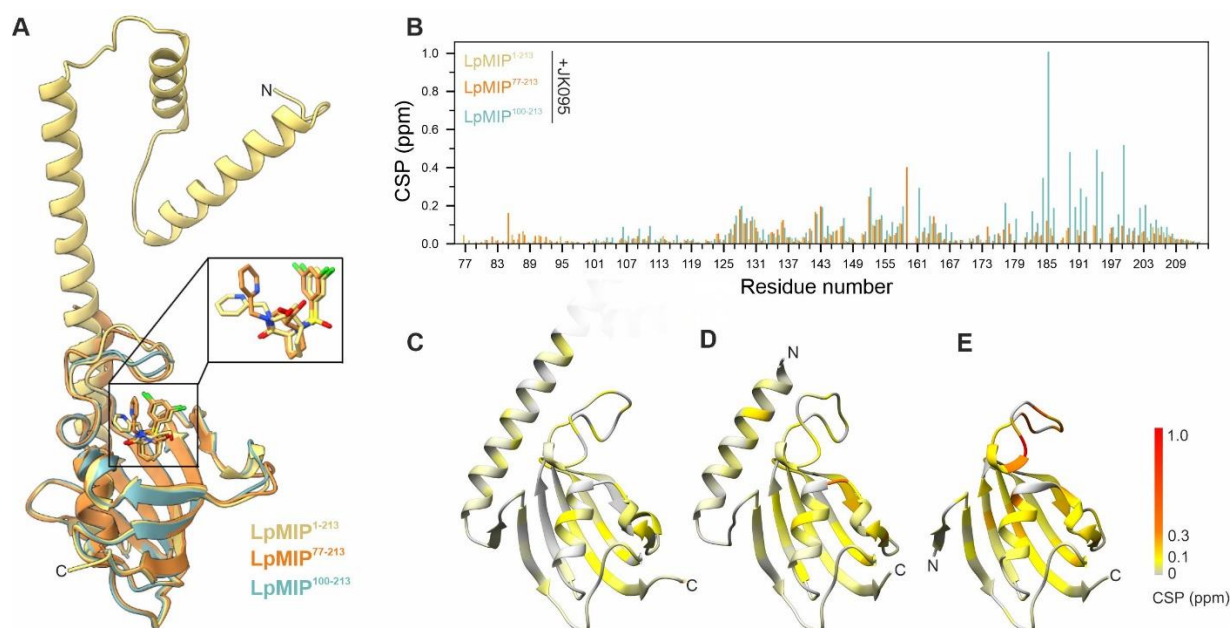


Fig. 5: Stalk helix affects interaction of *LpMIP* FKBP-like domain with a [4.3.1]-aza-bicyclic sulfonamide inhibitor.

(A) Overlay of the X-ray crystal structures of *LpMIP*¹⁻²¹³ (full-length), *LpMIP*⁷⁷⁻²¹³ and *LpMIP*¹⁰⁰⁻²¹³ co-crystallized with JK095 (PDB IDs: 8BJD, 8BK5, 8BK6). For the *LpMIP*¹⁻²¹³ homodimer, only one subunit is shown. *LpMIP*¹⁰⁰⁻²¹³ also crystallizes as a dimer, but no clear density for the ligand was obtained (for details see main text and compare Fig. S8). In the zoom-in, note that in *LpMIP*⁷⁷⁻²¹³, the hydroxymethyl group of JK095 was found to adopt two different conformations.

(B) Chemical shift perturbations in the FKBP-like domain of ¹⁵N-labeled full-length *LpMIP* (yellow), *LpMIP*⁷⁷⁻²¹³ (orange) and *LpMIP*¹⁰⁰⁻²¹³ (teal) upon titration with JK095. For better comparison between the three constructs, a unified scale normalized to the maximal shift value in the FKBP-like domain across all three data sets was used. (C-E) JK095-induced chemical shift perturbations within the FKBP-like domain plotted on crystal structures of full-length *LpMIP* (C), *LpMIP*⁷⁷⁻²¹³ (D) and *LpMIP*¹⁰⁰⁻²¹³ (E).

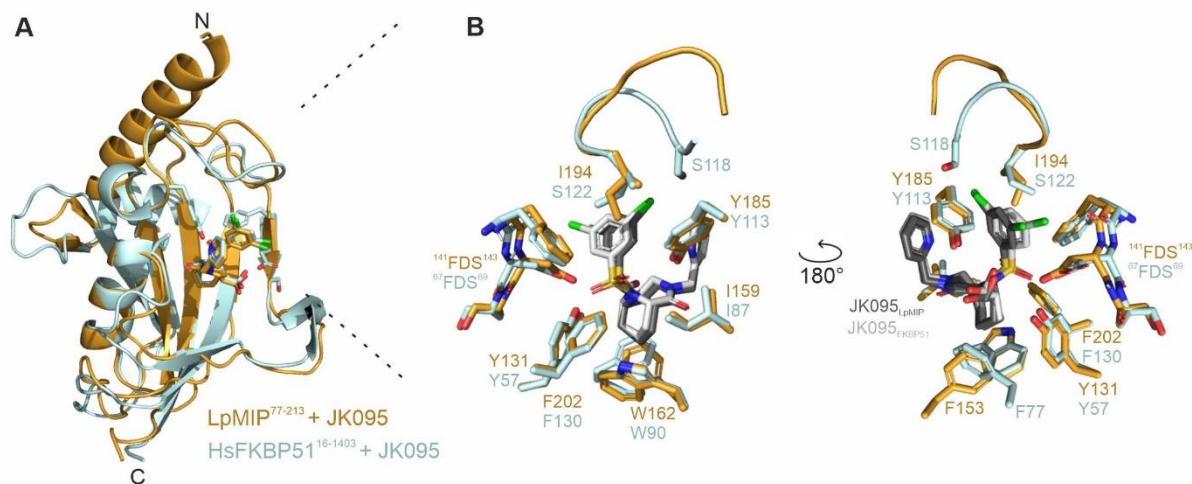


Fig. 6: Comparison of *LpMIP* and human FKBP51 in complex with the bicyclic inhibitor JK095.

(A) Overlay of the crystal structures of *LpMIP*⁷⁷⁻²¹³ (PDB: 8BK5, orange) and FKBP51¹⁶⁻¹⁴⁰ (PDB: 5OBK, cyan) in complex with the [4.3.1]-aza-bicyclic sulfonamide JK095.

(B) Zoom into the binding site. The relevant interacting residues are shown as sticks. JK095 is shown in dark (*LpMIP*⁷⁷⁻²¹³) or light (FKBP51¹⁶⁻¹⁴⁰) grey.

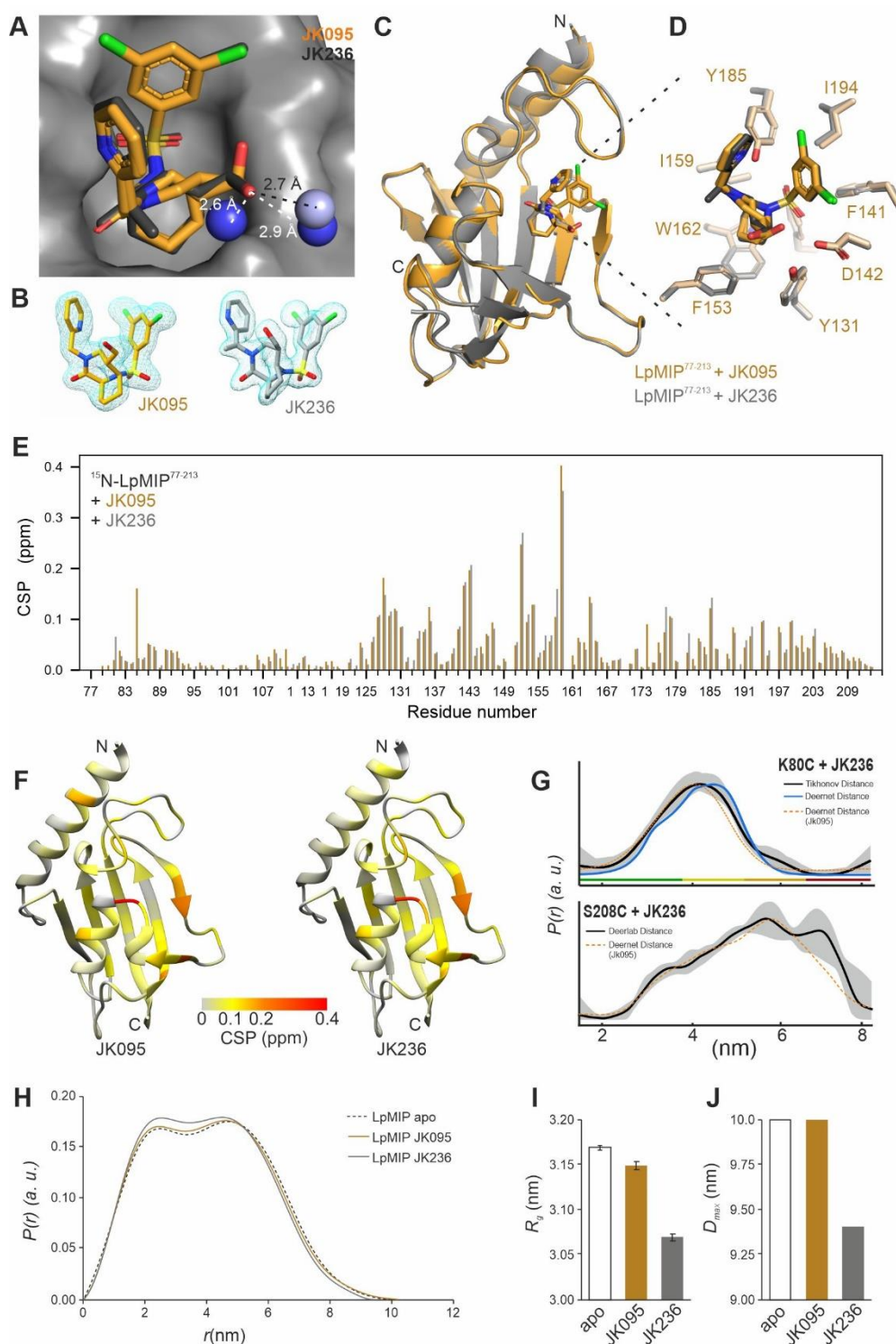


Fig. 7: Solvent exposed methyl group in [4.3.1]-aza-bicyclic sulfonamide inhibitor improves affinity for *LpMIP*⁷⁷⁻²¹³ through surface water displacement.

(A) Water molecules in the crystal structures of *LpMIP*⁷⁷⁻²¹³ with JK095 (PDB: 8BK5, dark blue spheres) and JK236 (PDB: 8BJE, light blue sphere). The additional methyl group in JK236 (pointing out of the paper plane) displaces one of the two water molecules that forms a hydrogen bond with the inhibitor's hydroxymethyl group.

Distances between crystallographic water and the inhibitors are indicated by white (JK095) and black (JK236) dashed lines.

(B) Electron densities for the two inhibitor molecules in the co-crystal structures with *LpMIP*⁷⁷⁻²¹³. Note that for JK095, the hydroxymethyl group adopts two conformations.

(C) Overlay of the crystal structures of *LpMIP*⁷⁷⁻²¹³ in complex with JK095 (PDB: 8BK5, orange) and its methylated derivative, JK236 (PDB: 8BJE, grey). For a structural comparison of the two molecules, see Scheme 1.

(D) Zoom into the binding site. The relevant interacting residues are shown as sticks.

(E) Relative NMR chemical shift perturbations (CSP) for JK095 (orange) and JK236 (grey) in comparison to the *apo* protein.

(F) Chemical shift perturbation shown in (E) mapped on the X-ray structure of *LpMIP*⁷⁷⁻²¹³ (PDB: 8BK5).

(G) Measured spin label distances using PELDOR/DEER spectroscopy for spin-labeled full-length *LpMIP* K80C (top) or S208C (bottom) with JK236. For better comparison, the distance distribution for JK095 (see Fig. 3) is indicated as a dashed orange line (without error margins).

(H) SAXS derived real-space pair-distance distribution functions, or $p(r)$ profiles, calculated for *LpMIP* in the absence (dashed line) or presence of JK095 (orange line) or JK236 (grey line) and

(I, J) resulting R_g and D_{max} values. $p(r)$ functions were scaled to an area under the curve value of 1.

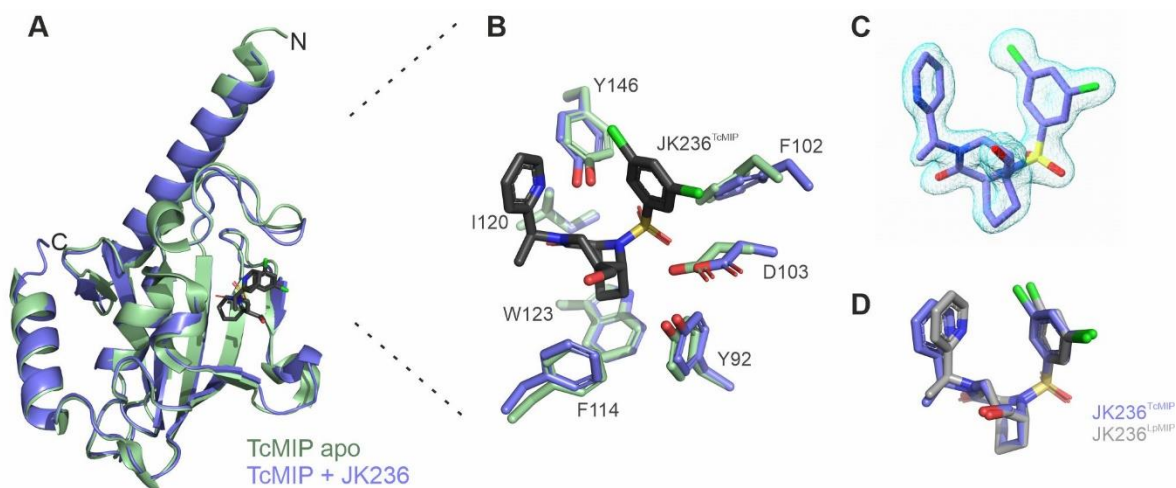


Fig. 8: *Trypanosoma cruzi* MIP in complex with a [4.3.1]-aza-bicyclic sulfonamide inhibitor.

(A) Overlay of the crystal structures of *apo* TcMIP (green, PDB: 1JVW) and JK236-bound TcMIP (blue, PDB: 8BK4).

(B) Active site residues in the *apo* or JK236-bound TcMIP. The ligand is shown in black.

(C) Electron density for JK236 bound to TcMIP. The 2Fo-Fc electron density maps are shown in light blue mesh at 3 σ .

(D) Comparison of the inhibitor binding stance in TcMIP (blue) and LpMIP⁷⁷⁻²¹³ (grey). For details, see also Fig. S9.